

DTIC FILE COPY

2

NAVAL POSTGRADUATE SCHOOL

Monterey, California

AD-A213 058



DTIC
ELECTE
OCT 02 1989
S B D

THESIS

REVIEW AND EVALUATION OF A
TURBOMACHINERY
THROUGHFLOW FINITE ELEMENT CODE

by

Peng Hian Yeo

June 1989

Thesis Advisor

Raymond P. Shreeve

Approved for public release; distribution is unlimited.

89 10 2 115

Unclassified

security classification of this page

REPORT DOCUMENTATION PAGE

1a Report Security Classification Unclassified			1b Restrictive Markings		
2a Security Classification Authority			3 Distribution Availability of Report		
2b Declassification Downgrading Schedule			Approved for public release; distribution is unlimited.		
4 Performing Organization Report Number(s)			5 Monitoring Organization Report Number(s)		
6a Name of Performing Organization Naval Postgraduate School		6b Office Symbol (if applicable) 61	7a Name of Monitoring Organization Naval Postgraduate School		
6c Address (city, state, and ZIP code) Monterey, CA 93943-5000			7b Address (city, state, and ZIP code) Monterey, CA 93943-5000		
8a Name of Funding Sponsoring Organization		8b Office Symbol (if applicable)	9 Procurement Instrument Identification Number		
8c Address (city, state, and ZIP code)			10 Source of Funding Numbers		
			Program Element No	Project No	Task No
			Work Unit Accession No		
11 Title (include security classification) REVIEW AND EVALUATION OF A TURBOMACHINERY THROUGHFLOW FINITE ELEMENT CODE. (Unclassified)					
12 Personal Author(s) Peng Hian Yeo					
13a Type of Report Engineer's Thesis		13b Time Covered From To		14 Date of Report (year, month, day) June 1989	
				15 Page Count 81	
16 Supplementary Notation The views expressed in this thesis are those of the author and do not reflect the official policy or position of the Department of Defense or the U.S. Government.					
17 Cesset Codes			18 Subject Terms (continue on reverse if necessary and identify by block number)		
Field	Group	Subgroup	Throughflow Analysis, Blockage, Rotor Tip Clearance Studies, Axial Flow Compressor		
19 Abstract (continue on reverse if necessary and identify by block number) The finite element code Q3DFLO'81 was evaluated to determine its suitability for use in a program to investigate axial compressor tip clearance effects. The code was first applied to Dring's fully comprehensive benchmark data set in order to validate the numerical modelling free of experimental uncertainties. It was then applied to the Naval Postgraduate School axial research compressor with which tip clearance effects were to be investigated experimentally. The evaluation identified both limitations in the code and limitations in the data which could be obtained in the experiment. It was recommended that provision be made to accommodate peripherally non-uniform flow effects (blockage) in the throughflow code calculation, and that provision be made to obtain adequate peripheral flow surveys in the experiment.					
20 Distribution Availability of Abstract <input checked="" type="checkbox"/> unclassified unlimited <input type="checkbox"/> same as report <input type="checkbox"/> DTIC users			21 Abstract Security Classification Unclassified		
22a Name of Responsible Individual Raymond P. Shreeve			22b Telephone (include Area code) (408) 646-2593		22c Office Symbol 61SF

DD FORM 1473, 84 MAR

83 APR edition may be used until exhausted
All other editions are obsolete

security classification of this page

Unclassified

Approved for public release; distribution is unlimited.

Review and Evaluation of a Turbomachinery
Throughflow Finite Element Code.

by

Peng Hian Yeo
Civilian, Singapore Ministry of Defence
B.Eng., University of Singapore, 1981

Submitted in partial fulfillment of the
requirements for the degree of

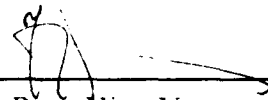
ENGINEER IN AERONAUTICAL ENGINEERING

from the

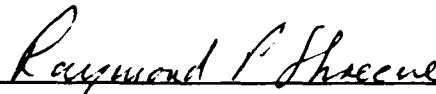
NAVAL POSTGRADUATE SCHOOL

June 1989

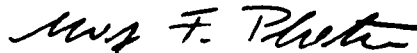
Author:


Peng Hian Yeo

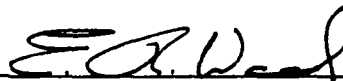
Approved by:



Raymond P. Shreeve, Thesis Advisor



Max F. Platzer, Second Reader



E. Roberts Wood, Chairman,
Department of Aeronautics and Astronautics



Gordon E. Schacher,
Dean of Science and Engineering

ABSTRACT

The finite element code Q3DFLO'81 was evaluated to determine its suitability for use in a program to investigate axial compressor tip clearance effects. The code was first applied to Dring's fully comprehensive benchmark data set in order to validate the numerical modelling free of experimental uncertainties. It was then applied to the Naval Postgraduate School axial research compressor with which tip clearance effects were to be investigated experimentally. The evaluation identified both limitations in the code and limitations in the data which could be obtained in the experiment. It was recommended that provision be made to accommodate peripherally non-uniform flow effects (blockage) in the throughflow code calculation, and that provision be made to obtain adequate peripheral flow surveys in the experiment.

Accession For	
NTIS GRA&I	<input checked="checked" type="checkbox"/>
DTIC TAB	<input type="checkbox"/>
Unannounced	<input type="checkbox"/>
Justification	
By	
Distribution/	
Availability Codes	
Dist	Avail and/or Special
A-1	



TABLE OF CONTENTS

I. INTRODUCTION	1
II. PRINCIPLES OF TURBOMACHINERY THROUGHFLOW MODELLING AND DESCRIPTION OF THE CODE	3
A. BACKGROUND	3
B. NON-AXISYMMETRIC NATURE OF THE REAL FLOW	4
C. EQUATION OF MOTION IN THE ABSOLUTE FRAME	4
D. EQUATION OF MOTION WITHIN A BLADE ROW	5
E. EQUATION OF MOTION IN THE RELATIVE FRAME	6
F. EQUATION OF MOTION USED IN Q3DFLO'81	7
G. SIMPLIFIED THROUGHFLOW MODEL OF Q3DFLO'81	7
H. BASIC FORMULATION OF Q3DFLO'81	8
III. ASSESSMENT OF THE CODE USING A BENCHMARK DATA SET	9
A. BACKGROUND	9
B. BLOCKAGE FACTORS IN THE Q3DFLO'81 FORMULATION	10
C. ASSESSMENT METHODOLOGY	11
D. INPUT DATA	12
E. EFFECT OF TANGENTIAL AERODYNAMIC BLOCKAGE ON THE THROUGHFLOW PREDICTION	13
F. CODE PREDICTION USING TWO DIMENSIONAL CASCADE DATA	14
G. OBSERVATIONS	15
IV. APPLICATION TO A MULTI-STAGE COMPRESSOR	16
A. BACKGROUND	16
B. EXPERIMENTAL SET-UP	16
C. EXPERIMENTAL MEASUREMENTS	17
D. MODELLING OF THE COMPRESSOR	19
E. EFFECT OF THE STRUT WAKES	19
F. ADAPTATION OF THE INLET FLOW CONDITION	20
G. RESULTS FOR THE ADAPTED INLET FLOW	21

H. COMPARISON OF THE OVERALL PERFORMANCE	22
I. EFFECT OF THE IGV EXIT FLOW UNDERTURNING	22
J. OBSERVATIONS	23
V. THE INVISCID BLADE-TO-BLADE SOLUTION	24
A. BACKGROUND	24
B. INPUT DATA AND SOLUTION	24
VI. CONCLUSIONS AND RECOMMENDATIONS	25
APPENDIX A. DERIVATION OF THE RELATIVE THROUGHFLOW EQUATION FOR Q3DFLO'S1	56
APPENDIX B. CALCULATION OF THE MIXED-OUT CONDITION FOR THE STRUT WAKES	62
LIST OF REFERENCES	65
INITIAL DISTRIBUTION LIST	67

LIST OF TABLES

Table 1.	EXPERIMENTAL FLOW AND PRESSURE COEFFICIENTS	18
Table 2.	BELLMOUTH VS INLET RAKE MEASUREMENTS OF FLOW RATE	20
Table 3.	DISPLACEMENT AND WAKE THICKNESSES AT STATION 1 . . .	21

LIST OF FIGURES

Figure 1. Stream Surfaces Through an Annular Blade Row	27
Figure 2. Velocities from a Rotating Row of Blades	28
Figure 3. Complex Flow Phenomena in a Compressor Rotor	29
Figure 4. Schematic Meridional Section of a Compressor Stage	30
Figure 5. Geometry of the Benchmark Compressor	31
Figure 6. Computational Mesh for the Benchmark Compressor	32
Figure 7. Spanwise Distribution of the Flow Properties at Station 1	33
Figure 8. Spanwise Distribution of the Loss Coefficient and Exit Flow Angle for the Second Rotor	34
Figure 9. Spanwise Distribution of the Loss Coefficient and Exit Flow Angle for the Second Stator	35
Figure 10. Spanwise Distribution of the Total Pressure Coefficient at Stations 7 and 13	36
Figure 11. Spanwise Distribution of the Relative Total Pressure Coefficient at Stations 1 and 7	37
Figure 12. Spanwise Distribution of the Static Pressure Coefficient at Stations 7 and 13	38
Figure 13. Spanwise Distribution of the Axial Velocity Component at Stations 7 and 13	39
Figure 14. Spanwise Distribution of the Absolute Flow Velocity at Stations 7 and 13	40
Figure 15. Spanwise Distribution of the Relative Flow Velocity at Stations 7 and 13	41
Figure 16. Spanwise Distribution of the Relative Flow Yaw Angle at Stations 1 and 13	42
Figure 17. Spanwise Distribution of the Absolute Flow Yaw Angle at Station 7 ..	43
Figure 18. Radial Section of the NPS Compressor	44
Figure 19. Spanwise Distribution of the Flow Properties Measured Ahead of the Inlet Guide Vane	45
Figure 20. Computational Mesh for the NPS Compressor	46
Figure 21. Compressor Strut Section	47
Figure 22. Spanwise Distribution of the Mixed-out Flow Properties Calculated	

Ahead of the Inlet Guide Vane	48
Figure 23. Variation of the Compressor Pressure Rise Coefficient with Flow	
Coefficient	49
Figure 24. Spanwise Distribution of the Flow Angle from the Inlet Guide Vane ..	50
Figure 25. Effect of the Inlet Guide Vane Flow Underturning on the Pressure Rise	
Coefficient	51
Figure 26. Profile of the Rotor Tip Section	52
Figure 27. Computational Mesh for the Blade-to-Blade Solution	53
Figure 28. Iso-pressure Lines from the Blade-to-Blade Solution	54
Figure 29. Pressure Coefficients from the Blade-to-Blade Solution	55
Figure 30. Relationship between Blade Surface Angles and Body Forces	61
Figure 31. Schematic for Constant Area Mixing Calculation for the Strut Wakes ..	64

LIST OF SYMBOLS

S_m	Surface of Revolution
S_b	Blade surface
S_1, S_2	Stream surfaces
∇	Gradient operator in the absolute frame of reference
∇_R	Gradient operator in the relative frame of reference
\vec{V}	Absolute velocity
V_m	Meridional velocity component
V_θ	Tangential velocity component
V_r	Radial velocity component
V_z	Axial velocity component
t	Time
P	Static pressure
ρ	Density
g	Gravitational acceleration
Z	Potential height
\vec{F}_f	Friction force
h	Static enthalpy
T	Static temperature
S	Entropy
H	Total enthalpy
\vec{W}	Relative velocity
W_z	Axial relative velocity component
W_θ	Tangential relative velocity component
W_r	Radial relative velocity component
$\vec{\omega}$	Rotor angular velocity
\vec{R}	Radius vector
I	Rothalpy
$\vec{i}, \vec{j}, \vec{k}$	Unit directional vectors of the rectangular co-ordinate system

x, y, z	Co-ordinate components of the rectangular co-ordinate system
$\bar{i}, \bar{i}_\theta, \bar{i}_z$	Unit directional vectors in the cylindrical co-ordinate system
\bar{F}_b	Body force
$F_{b,\theta}$	Tangential component of the body force
$F_{b,z}$	Axial component of the body force
$F_{b,r}$	Radial component of the body force
b	Tangential blockage factor
ψ	Stream function
\dot{m}	Massflow rate
δ_1^*	Boundary layer displacement thickness at the hub
δ_2^*	Boundary layer displacement thickness at the shroud
ϕ	Flow coefficient
IGV	Inlet guide vane
ρ_{igv}	Density at the inlet of the IGV
A_{igv}	Annular area at the inlet of the IGV
U_m	Rotor mid-span peripheral speed
Π	Pressure rise coefficient
ΔP_s	Static pressure rise across the stages measured at the shroud
T_{bell}	Static temperature measured at the bellmouth
P_{OT}	Total pressure measured at the bellmouth
P_{OS}	Static pressure measured at the bellmouth
ρ_{bell}	Density calculated at the bellmouth
V_{bell}	Axial velocity calculated at the bellmouth
d_{bell}	Bellmouth internal diameter
A_{bell}	Bellmouth cross-sectional area
$T_{i,igv}$	Static temperature measured ahead of the IGV inlet
$P_{t,igv}$	Total pressure measured ahead of the IGV inlet
$P_{s,igv}$	Static pressure measured ahead of the IGV inlet
ρ_{igv}	Density calculated at the measurement plane ahead of the IGV inlet
P_{i1}	Static pressure measured at the shroud ahead of the first rotor
P_{s2}	Static pressure measured at the shroud aft of the second stator
N	Rotor revolutions per minute

R_n	Mean radii of the compressor annulus
V_x	Axial velocity component
\dot{m}_{bell}	Massflow rate measured at the bellmouth
\dot{m}_{IGV}	Massflow rate measured at the IGV inlet
s	Pitch
δ^*	Wake thickness
V_1	Flow velocity before wake diffusion
V_2	Mixed-out flow velocity
P_1	Static pressure before wake diffusion
P_2	Mixed-out static pressure
P_{t1}	Total pressure before wake diffusion
P_{t2}	Mixed-out total pressure

ACKNOWLEDGMENT

I wish to express my gratitude to Prof Charles Hirsch at Vrije University in Brussels for his guidance on the use of Q3DFLO'81 code, whilst he was at the Naval Postgraduate School (NPS), Monterey, in Aug 1988. I also wish to thank Mr Moyle Ian N., research associate at the NPS Turbopropulsion Laboratory for sharing his in-depth knowledge of the NPS compressor test rig. Thanks also go to Dr Robert P. Dring at United Technologies Research Center for his guidance on the use of the benchmark compressor data base and his accounts of the historical treatment of the tangential aerodynamic blockage.

To my wife, Lay-Lian, I would like to say thank you for her encouragement and typing of this thesis.

Finally, I am indebted to Prof Raymond P. Shreeve, who is my thesis advisor, for introducing me to the field of advanced treatment of turbomachinery flowfield computation. His advice and close supervision are instrumental to the completion of this thesis.

I. INTRODUCTION

The effect of finite rotor tip clearance on the operating characteristics of compressors is not well understood. An investigation is currently underway at the Turbopropulsion Laboratory of the Naval Postgraduate School (NPS) to explore the interaction of the tip leakage flow with the rotor passage flow, and to identify parameters which control the effect of tip clearance on compressor performance. Experiments are conducted on a 36 inch diameter low speed axial flow compressor test rig. The compressor has three repeating stages and is currently configured with two stages of symmetrical blading. Measurements of the compressor performance are obtained using fixed probes and rakes, a flow nozzle and a torque meter. Flow survey data are obtained between blade rows using pneumatic probes. Rotor exit conditions are measured using hot-wire probes. Also, using high-response semi-conductor pressure transducers and conditional sampling, the pressure field on the axisymmetric surface across the rotor tip is mapped. A complete description of the three dimensional flowfield within the compressor is desired. However, for each type of flow survey, the coverage of the compressor annulus is limited by the access holes provided in the heavy compressor case-wall. Since the experimental program would be expected to develop a modification to current models for tip-clearance effects on throughflow development, a computational code incorporating a case-wall boundary layer calculation was needed with which to obtain predictions of the experimental conditions. The code would then provide a vehicle in which to incorporate a change in the tip-flow model.

The finite element code Q3DFLO'81 was examined with this purpose in mind. The code was installed on the NPS mainframe IBM 370-3033 computer in 1983 by its originator, Professor Charles Hirsch, and was used successfully at that time.

The purpose of the present evaluation was specifically to determine the suitability of the code for the tip-clearance application, for which the case-wall boundary layer modelling would be a significant consideration. The evaluation was performed in two steps. First, the code was applied to a fully documented, 'benchmark', test case wherein completely detailed flow field information was available in addition to the geometry and the controlled boundary conditions. The findings from this effort are described in Chapter III. Then, with a developed appreciation of the degree to which the code described actual compressor flow conditions, the code was applied to the NPS

compressor geometry. A comparison was made of code predictions with the pressure-rise performance measured experimentally. The results are described in Chapter IV. In order to provide a comparison with measured rotor-tip pressure contours, blade-to-blade calculations were also made at two compressor throughflow rates. An example is described in Chapter V. Conclusions and recommendations following both phases of the evaluation are given in Chapter VI. In general, it was found that the most significant limitation of the code for the desired application lies in the absence of a mechanism to input peripherally non-uniform flow effects, which are certainly always present in the machine. The need to obtain complete peripheral flow surveys in the experimental program was also identified.

Before detailing the results of the evaluation, a review of the theoretical background and modeling on which the code is based, is given in Chapter II.

II. PRINCIPLES OF TURBOMACHINERY THROUGHFLOW MODELLING AND DESCRIPTION OF THE CODE

A. BACKGROUND

Q3DFLO'81 is a Finite Element code developed by Prof Charles Hirsch and his coworkers at Vrije University in Brussels for computing the complex flowfield in a turbomachine and its associated axisymmetric ducting. The formulation of the computational model of the flowfield to its final form for numerical coding is described in references 1 and 2. Reference 1 describes all available approaches to the treatment of turbomachinery flowfields and derivative computational methods, including those used in the development of Q3DFLO'81. Reference 2 is a summary of the key equations programmed in the Q3DFLO'81 computational code, which was the focus of the present study.

Since the two references were intended for specialists in the field of turbomachinery flow modelling, no detailed algebraic operations were provided from one step to another. For a newcomer like the author, it was not easy to follow the logic and the mathematical language used in the presentation. To complicate matters, the equation of motion can be written in several different forms, although all are equivalent. Typically, for a flow in an annulus region, the equation is normally expressed with respect to an absolute frame of reference and within the blade to blade region with respect to a relative frame of reference. However, in the Q3DFLO'81 formulation, the equation of motion contains variables from both the absolute frame and the relative frame, in the same equation!

The objective of this chapter therefore is to review the development of the equations which are the basis of flowfield computations in turbomachinery. The relationship between the various forms of the equation of motion is shown and the detailed algebraic operations that were omitted in summarizing the development of the Q3DFLO'81 in reference 2 are described here. Detailed derivation of equations which are available in texts and references will not be repeated. In such situations, only the key equations and their physical interpretations are presented. It is hoped that this will give similar newcomers a basic understanding before attempting the advanced materials in reference 1.

B. NON-AXISYMMETRIC NATURE OF THE REAL FLOW

Figure 1 shows a blade row with radial leading and trailing edges and 4 families of surfaces; namely, surfaces of revolution S_m , blade surfaces S_b and stream surfaces S_1 and S_2 . S_m is the axisymmetric surface generated by a generatrix m , as it rotates 360° about the axis. S_b is simply the blade surface. Suppose a row of dyed particles is initially held along the edge A-P-C and another row along B_2 -P- B_1 at the inlet. When these particles are released, it is found that:

- The row of particles initially along A-P-C does not follow the blade surface S_b . They instead follow the stream surface S_2 contrary to one's expectation.
- Similarly, the row of particles initially along B_2 -P- B_1 does not follow the axisymmetric surface S_m . Instead they follow the stream surface S_1 .

These observations have been verified by experiments. A flow through stationary or rotating cascades cannot be axisymmetric if the flow is to exert a moment on the blades. [Ref. 3: pp. 216]

In the annulus region between the blade rows, the flow can be considered to be axisymmetric after the wake has mixed out. In the formulation of through flow analysis, the flow within the blade row is also very often assumed to be axisymmetric to simplify the mathematical model i.e. surfaces S_m will coincide with S_1 and S_b with S_2 . This assumption is also adopted in the following derivation. However, this assumption causes discrepancies in the velocity components and flow angles between experimental measurement and throughflow modelling results. These discrepancies can be corrected by incorporating a factor known as the tangential blockage. This is dealt with in the next chapter.

C. EQUATION OF MOTION IN THE ABSOLUTE FRAME

The fundamental equation of fluid motion can be expressed as

$$\frac{\partial \vec{V}}{\partial t} + \vec{V} \cdot \nabla \vec{V} = -\frac{\nabla P}{\rho} - \nabla(gZ) + \vec{F}_f \quad \{1\}$$

for viscous, compressible or incompressible fluids.

In turbomachinery applications, the equation of motion is very often expressed in terms of enthalpy instead of pressure. This is done in 2 steps. First, use the vector identity

$$\vec{V} \cdot \nabla \vec{V} = \nabla\left(\frac{V^2}{2}\right) - \vec{V} \times \nabla \times \vec{V} \quad \{2\}$$

Second, introduce the relationship between two thermodynamic states along the path of a fluid particle

$$\nabla h - T\nabla S = \frac{\nabla P}{\rho} \quad \{3\}$$

Using Eq. (2) and Eq. (3), Eq. (1) becomes

$$\frac{\partial \vec{V}}{\partial t} + \nabla \left(\frac{V^2}{2} \right) - \vec{V} \times \nabla \times \vec{V} = T\nabla S - \nabla h - \nabla(gZ) + \vec{F}_f \quad \{4\}$$

Re-arranging,

$$\frac{\partial \vec{V}}{\partial t} + \nabla \left(h + \frac{V^2}{2} + gZ \right) = T\nabla S + \vec{V} \times \nabla \times \vec{V} + \vec{F}_f \quad \{5\}$$

The total enthalpy is defined as

$$H = h + \frac{V^2}{2} + gZ \quad \{6\}$$

Using Eq. (6), Eq. (5) becomes

$$\frac{\partial \vec{V}}{\partial t} + \nabla H = T\nabla S + \vec{V} \times \nabla \times \vec{V} + \vec{F}_f \quad \{7\}$$

The detailed derivation of Eqn (2) and (3) is given in reference 3. For a steady and isentropic flow, Eq. (7) reduces to

$$\nabla H = \vec{V} \times \nabla \times \vec{V} \quad \{8\}$$

If $\nabla H = 0$, the fluid is either non-rotational or the vorticity is parallel to the particle velocity.

D. EQUATION OF MOTION WITHIN A BLADE ROW

Figure 2 shows the outlet flow of a constant speed rotating rotor with a relative velocity profile represented by the vectors W_1 to W_6 . A stationary observer attached to the stator blade row looking at the rotor outlet will see a non-steady velocity profile represented by the vectors V_1 to V_6 which vary in both magnitude and direction. It is clear that Eq. (7) is not useful for describing the flow within the rotor region, as the term

$\frac{\partial \vec{V}}{\partial t}$ cannot be neglected nor determined. Hence, it is more useful to adopt a rotating frame of reference that rotates at the same speed as the rotor for describing the flow within the rotor blade row. [Ref. 3: pp. 110,111]

E. EQUATION OF MOTION IN THE RELATIVE FRAME

The equation of motion with respect to the rotating frame can be obtained directly from Eq. (1) by replacing the absolute velocity by the relative velocity using

$$\vec{V} = \vec{W} + \vec{\omega} \times \vec{R} \quad \{9\}$$

and taking all changes with respect to the relative system (i.e. ∇_R in place of ∇ and $\frac{\partial_R}{\partial t}$ in place of $\frac{\partial}{\partial t}$). The left hand side (LHS) of Eqn (1) can be expressed as

$$\begin{aligned} \frac{\partial \vec{V}}{\partial t} + \vec{V} \cdot \nabla \vec{V} &= \frac{\partial}{\partial t} (\vec{W} + \vec{\omega} \times \vec{R}) + (\vec{W} + \vec{\omega} \times \vec{R}) \cdot \nabla (\vec{W} + \vec{\omega} \times \vec{R}) \\ &= \frac{\partial_R \vec{W}}{\partial t} + \vec{W} \cdot \nabla_R \vec{W} + 2\vec{\omega} \times \vec{W} - \nabla_R \left(\frac{\omega^2 R^2}{2} \right) \end{aligned} \quad \{10\}$$

and Eq. (1) becomes

$$\frac{\partial_R \vec{W}}{\partial t} + \vec{W} \cdot \nabla_R \vec{W} + 2\vec{\omega} \times \vec{W} - \nabla_R \left(\frac{\omega^2 R^2}{2} \right) = -\frac{\nabla_R P}{\rho} - \nabla_R (gZ) + \vec{F}_f \quad \{11\}$$

The detailed derivation of Eqn (10) is given in reference 3.

Again using the vector identity of Eqn (2) and the thermodynamic relationship of Eqn (3) in the relative frame, Eqn (11) becomes

$$\begin{aligned} \frac{\partial_R \vec{W}}{\partial t} + \nabla_R \left(\frac{W^2}{2} \right) - \vec{W} \times \nabla_R \times \vec{W} + 2\vec{\omega} \times \vec{W} - \nabla_R \left(\frac{\omega^2 R^2}{2} \right) \\ = T \nabla_R S - \nabla_R h - \nabla_R (gZ) + \vec{F}_f \end{aligned} \quad \{12\}$$

Re-arranging,

$$\frac{\partial_R \vec{W}}{\partial t} + \nabla_R \left(h + \frac{W^2}{2} + gZ - \frac{\omega^2 R^2}{2} \right) = T \nabla_R S + \vec{W} \times (\nabla_R \times \vec{W} + 2\vec{\omega}) + \vec{F}_f \quad \{13\}$$

With the rothalpy defined as

$$I = h + \frac{W^2}{2} + gZ - \frac{\omega^2 R^2}{2} \quad \{14\}$$

the equation of motion in the relative frame is then

$$\frac{\partial_R \vec{W}}{\partial t} + \nabla_R I = T \nabla_R S + \vec{W} \times (\nabla_R \times \vec{W} + 2\vec{\omega}) + \vec{F}_f \quad \{15\}$$

For a steady and isentropic flow within the rotor and with the rothalpy constant, Eq. (15) reduces to

$$\vec{W} \times (\nabla_R \times \vec{W} + 2\vec{\omega}) = 0 \quad \{16\}$$

Physically, this means that the flow is rotational with respect to the rotating frame and the relative vorticity is opposite to and equal to twice the rotor rotation.

However, it should be pointed out that the assumption of steady relative flow, though frequently made in turbomachinery calculations, is true only if the inlet flow to the rotor is uniform in the tangential direction; i.e. the wakes of any upstream blade rows must have mixed out. Hirsch [Ref. 1: pp. 53] states that in a real flow, "the viscous interactions and unsteadiness, which are always present to some degree in turbomachinery flow, introduce variations in rothalpy along the flow path."

F. EQUATION OF MOTION USED IN Q3DFLO'81

An alternative form of the equation of motion for steady, relative, three-dimensional flow which is used in Q3DFLO'81 involves both relative and absolute velocity components; namely,

$$\nabla_R I = T \nabla_R S + \vec{W} \times (\nabla \times \vec{V}) + \vec{F}_f \quad \{17\}$$

Eq. (17) is the same as Eq. (15) for a steady flow, except that the term $(\nabla_R \times \vec{W} + 2\vec{\omega})$ is expressed in terms of $(\nabla \times \vec{V})$.

G. SIMPLIFIED THROUGHFLOW MODEL OF Q3DFLO'81

Figure 3 shows the characteristics of an actual flow within the blade passage of a rotor. The flow is highly three-dimensional with strong corner vortices generated at the corners between the blade and hub and between the blade and shroud. There is also a secondary flow surrounding the primary core flow. However, the Q3DFLO'81 throughflow uses a simplified axisymmetric flow model, and the three-dimensional

details are removed (accounted for) by taking the density average of the flow over the blade spacing at each spanwise position.

In assuming the flow to be axisymmetric through blade row, the effects of the blades themselves must be introduced into the equation of motion as a body force. The equation of motion (Eq. 17) becomes

$$-\vec{W} \times (\nabla \times \vec{V}) = T \nabla_R S - \nabla_R I + \vec{F}_b + \vec{F}_f \quad \{18\}$$

H. BASIC FORMULATION OF Q3DFLO'81

The basic steps of the formulation of Q3DFLO'81 throughflow model are described in reference 2. The throughflow equation known as the Radial Equilibrium Equation that is solved in the Q3DFLO'81 code for the flow within the rotor is

$$\begin{aligned} & \frac{\partial}{\partial r} \left(\frac{1}{\rho r b} \frac{\partial \psi}{\partial r} \right) + \frac{\partial}{\partial z} \left(\frac{1}{\rho r b} \frac{\partial \psi}{\partial z} \right) = \\ & \frac{(W_z + W_\theta \tan \beta) \left(\frac{\partial I}{\partial r} - T \frac{\partial S}{\partial r} \right) + (W_\theta \tan \eta - W_r) \left(\frac{\partial I}{\partial z} - T \frac{\partial S}{\partial z} \right)}{W^2} \\ & - \frac{1}{r} \left(\tan \beta \frac{\partial(r V_\theta)}{\partial r} + \tan \eta \frac{\partial(r V_r)}{\partial z} \right) \end{aligned} \quad \{19\}$$

Eq. (19) is derived from Eq. (18). Details of the derivation are given in Appendix (A).

For the flow within the stator, Eq. (19) is still applicable. As the stator is stationary, the relative velocity components are replaced by the absolute velocity components and the rothalpy is replaced by the enthalpy.

However, for the flow within the annular region without blades such as the annular space between a rotor and stator blade rows, Eq. (19) is not applicable. The inviscid equation of motion is used in such regions. The formulation of the form of equation of motion that is solved in Q3DFLO'81 for the flow in blade-free annular regions is given in reference 2.

Figure 4 shows the boundary conditions applied to the throughflow calculation. The last station must be normal to the meridional velocity.

The radial equilibrium equations for the flow within the blade row and the annular region are non-linear. They are solved by the finite element method using an iterative procedure. The details of the numerical method are also described in reference 2.

III. ASSESSMENT OF THE CODE USING A BENCHMARK DATA SET

A. BACKGROUND

The set of radial equilibrium equations, which is solved in Q3DFLO'81 is only one of three major ingredients in the code. Q3DFLO'81 incorporates an endwall boundary layer calculation which (optionally) can be coupled into the radial equilibrium solution procedure. The flow is then solved iteratively to account for the effect of boundary layer and tip clearance losses. Like all other throughflow codes, Q3DFLO'81 also makes use of correlations of two dimensional cascade data for the loss coefficient and flow turning angle. Consequently, the ability to predict the performance of an axial compressor using Q3DFLO'81 depends not only on the simplified modelling of the physical flow and the accuracy of the numerical method but also on the applicability and accuracy of the two dimensional cascade data.

Comparisons of predictions using Q3DFLO'81 with experimental data on axial flow compressors were carried out at the Naval Postgraduate School during 1983 and 1984. It was concluded at that time that the code was able to predict the general behaviour of the flowfield with certain discrepancies [Ref. 4]. However, the experimental data in each application were not complete enough to enable the evaluation of each aspect of the code independently, such as the axisymmetry assumption in modelling the physical flow and the use of two dimensional cascade data for correlating the losses across the blade row. Furthermore, the spanwise static pressure distribution, which is the most sensitive indicator of accuracy in applying throughflow codes, was not available from the experiments.

In 1985, under the sponsorship of the Naval Air System Command, completely detailed flowfield surveys obtained in a five feet diameter two stage axial flow compressor at United Technologies Research Center (UTRC) were used to assess the accuracy and utility of throughflow codes for predicting compressor flow fields and compressor performance. The relevant parameters of the flowfield required for a comparison with code predictions, such as the spanwise variation of the total pressure loss coefficient, flow turning angle and tangential aerodynamic blockage, were obtained from the surveys. Dring and Joslyn [Ref. 5: pp. 56-64] used the reduced experimental data in a throughflow finite element code developed by Habashi and Youngson. They concluded that an accurate description of the tangential aerodynamic blockage, resulting

from the non-axisymmetry of the physical flow and the presence of wakes, was essential if the flow field was to be predicted accurately. The detailed set of measurements was subsequently made available as a benchmark data set for the assessment of other throughflow codes in reference 5.

With the complete survey data available as inputs, the Q3DFLO'81 code can be run on the benchmark compressor without accessing the two dimensional cascade loss and deviation correlations and the endwall boundary layer subroutines. This enables the effects of blade wakes and accuracy of the axisymmetric flow assumption to be assessed by running the code with and without accounting for the tangential aerodynamic blockage. In the process, the accuracy of the code's numerical method can be examined.

The benchmark axial flow compressor had extensive hub corner stall in the second stage stator. Although cascade data are not appropriate for correlating the losses and exit deviation angle across the blade row of compressor with extensive region of stall, it is interesting to see how different, quantitatively, the predictions will be using the correlation subroutine in Q3DFLO'81, which is based on two dimensional cascade data, compared to the use of actual survey data. This interest arises because Dring has observed the occurrence of hub corner stall in all the configurations tested at UTRC.

B. BLOCKAGE FACTORS IN THE Q3DFLO'81 FORMULATION

There are 2 types of blockage involved in throughflow modelling; namely, endwall blockage and tangential (two dimensional) blockage [Refs. 2,6]. Endwall blockage accounts for the reduction in throughflow area due to the displacement thickness of the boundary layer along the shroud and hub surfaces. Q3DFLO'81 accounts for the effect of endwall blockage by applying the endwall boundary conditions

$$\psi = -\delta_1^*(\rho V_m r)_{hub}$$

and

$$\psi = \frac{\dot{m}}{2\pi} + \delta_2^*(\rho V_m r)_{shroud}$$

at the hub and case walls respectively. Here, \dot{m} is the massflow rate and δ_1^* and δ_2^* are the boundary layer displacement thicknesses at the hub and shroud respectively.

The tangential blockage, $(1 - b)$, accounts for the reduction in the effective annulus area in the circumferential direction. The tangential blockage varies as a function of radius. Dring [Ref. 5: pp. 11] states that "the blockage $(1 - b)$ reflects the fraction of the

circumference not available to the inviscid throughflow." Tangential blockage can be mechanical or aerodynamic. Mechanical blockage occurs within the blade row due to the airfoil tangential thickness. Aerodynamic blockage occurs both within the blade row as well as in the annulus region between blade rows. Within the blade row, the aerodynamic blockage results from the displacement thicknesses of the boundary layers along the blade surfaces and the departure from axisymmetry. In the annulus region, the aerodynamic blockage is due to blade wakes and non-axisymmetries such as corner stall.

Q3DFLO'81 accounts for the tangential blockage by defining the axial (W_z) and radial (W_r) velocity components in its governing equation as

$$W_z = \frac{1}{\rho r b} \frac{\partial \psi}{\partial r}$$

and

$$W_r = - \frac{1}{\rho r b} \frac{\partial \psi}{\partial z}$$

However, Q3DFLO'81 only computes the tangential blockage ($1 - b$) due to the mechanical blockage within the blade rows, and does not include aerodynamic blockage. There is no provision for introducing the aerodynamic blockage as input data.

C. ASSESSMENT METHODOLOGY

Measured values of deviation angle and loss coefficients can be used as inputs to the code. Consequently, the applicability of the correlation expressions for the losses and deviation angle that are contained in Q3DFLO'81, to the prediction of the performance of a compressor with a large stall region, can be assessed. First, the code can be run inputting measured quantities from the benchmark data set, and then run again using the correlation subroutines. Both runs will use the same geometrical data and will have the same inlet conditions.

An assessment of the effect of including tangential aerodynamic blockage cannot be done in a straight forward manner since Q3DFLO'81 does not have provisions for introducing tangential aerodynamic blockage as input data. What can be done is to use an average value for the tangential aerodynamic blockage (given by reference 5 on page 21 as a mass-average value) and equate it to the equivalent endwall blockage, which the code can accept as an input.

This approach, although not physically correct, does give an indication of the effect of the tangential aerodynamic blockage on the throughflow prediction. In a broad sense, both types of blockages are similar in their effect. They both increase the meridional velocity component in the throughflow. From the results presented by Dring and Joslyn [Ref. 5: pp. 49,99,102], one can conclude that, in the absence of a detailed description of the radial variation in the tangential aerodynamic blockage, a uniform tangential aerodynamic blockage (an average value) produces much better results than by not including the tangential aerodynamic blockage at all.

Three cases were run on the benchmark compressor using Q3DFLO'81. Cases 1 and 2 were run using the measured values of loss and deviation angle. However, Case 1 was run with no tangential aerodynamic blockage and Case 2 with an equivalent tangential aerodynamic blockage added to the case-wall. The results of Cases 1 and 2 are compared with the benchmark compressor experimental results to assess the effect of including tangential aerodynamic blockage on the prediction. Case 3 was run using the Q3DFLO'81 correlation subroutines and with the same equivalent tangential aerodynamic blockage added to the case-wall as for Case 2. The Case 3 prediction was compared to those of Cases 1 and 2. In all the three cases, the endwall boundary layer computation in the code was not used.

D. INPUT DATA

The annulus of the benchmark compressor was cylindrical. The radius of the hub and tip were 24 ins and 30 ins respectively. The airfoils of the rotor and stator were NACA 65 series with circular arc camber lines. Figure 5 and Figure 6 show a schematic and the computational mesh for the benchmark compressor respectively. Only the second stage rotor and stator were modelled. This was because the detailed measurements were provided for the second stage and furthermore, Q3DFLO'81 is limited by the grid capacity and could not model the whole compressor and maintain adequate resolution near the walls. A total of 15 stations was used. Station 1, the inlet station to the second stage, is located mid-way between the first stage stator trailing edge and the second stage rotor leading edge. Stations 2 and 6 correspond to the second stage rotor leading and trailing edges respectively, and Stations 8 and 12 to the second stage stator leading and trailing edges respectively. The code predictions and benchmark measurements were compared at Stations 7 and 13, which correspond to Stations 4 and 5 in reference 5.

A total of 11 axial grid lines (which is the maximum permitted by Q3DFLO'81) was used. The streamlines were also clustered towards the shroud by using a repartition factor of 0.1. This emphasis on the tip region was necessitated by the abrupt variation in the benchmark loss coefficient near the casewall. Figure 7 shows the distributions of the velocities and total pressure as a function of radius at Station 1, which were input for all three cases. Figure 8 and Figure 9 show the distributions of the benchmark loss coefficient and exit flow angle as a function of radius for the second stage rotor and stator, which were input for Cases 1 and 2.

Several points are noted. The benchmark data are given in terms of non-dimensional quantities. For use in Q3DFLO'81, the data were converted to the dimensional form in metric units. A Standard Day of 15° C and 1.01325 bar was chosen as the inlet condition of the compressor to calculate the mass flow rate and the velocities. The loss coefficients given in the benchmark data are specified with respect to the mid-span wheel speed. For Q3DFLO'81, the loss coefficients were re-calculated with respect to the benchmark rotor inlet relative velocity and the stator inlet absolute velocity at their specified radial positions, for the rotor and stator respectively. In Q3DFLO'81, the aerodynamic input data are limited to 10 radial points for each variable. Since 18 to 20 points were specified in the benchmark data set for each variable, ten points were carefully selected such that they represented the macro variation as closely as possible.

E. EFFECT OF TANGENTIAL AERODYNAMIC BLOCKAGE ON THE THROUGHFLOW PREDICTION

Figure 10 through Figure 17 compare the Q3DFLO'81 code predictions for Cases 1 and 2 with the experimental results. The comparisons are made at Stations 7 and 13 for the following parameters:

- Total pressure coefficient
- Relative total pressure coefficient
- Static pressure coefficient
- Axial velocity component
- Absolute flow velocity
- Relative flow velocity
- Relative flow yaw angle
- Absolute flow yaw angle

Q3DFLO'81 outputs the pressure and flow velocity in metric units; namely, bar, and meter per second. These parameters, shown plotted in Figure 10 to Figure 17, were non-dimensionalised using the mid-span wheel speed.

At Station 7, Figure 10 through Figure 17 show that the predictions of Cases 1 and 2 are very similar. It can be seen that Case 2 agrees slightly better than Case 1 with the benchmark data in both magnitudes and overall trends.

At Station 13, Figure 12, Figure 13 and Figure 16, however show that there are significant differences in the predictions of static pressure, axial velocity and relative flow yaw angle between Case 1 and Case 2. The prediction of Case 2 agrees very well with the benchmark data, but not Case 1. Case 1 shows appreciably higher static pressure and relative flow yaw angle and lower axial velocity.

The agreement at Station 7 and disagreement at Station 13 between Case 1 and Case 2 are, almost certainly, the result of the tangential aerodynamic blockage introduced at these stations in Case 2. The tangential aerodynamic blockage is 1.4 percent at Station 7 compared to 4.7 percent at Station 13. For a constant massflow rate, the absence of 1.4 percent area blockage at station 7 in Case 1 causes a slight reduction in the axial velocity which results in only a slight increase in static pressure and absolute flow yaw angle as can be seen in Figure 12 and Figure 17. However, the effect of ignoring the 4.7 percent blockage at Station 13 in Case 1 is clearly significant. It causes a marked reduction in the predicted axial velocity, which results in a significant increase in the static pressure and relative flow yaw angle.

F. CODE PREDICTION USING TWO DIMENSIONAL CASCADE DATA

Figure 10 through Figure 17 also show the predictions for Case 3, which uses the code's correlations of cascade data, rather than measured data, for computing loss and deviation angle. The Q3DFLO'81 endwall boundary layer part of the code was not used because of the limited resolution in the benchmark data and difficulties in starting the endwall boundary layer calculation in the middle of the compressor. Clearly, the most meaningful evaluation of the accuracy of the cascade correlation will come from a comparison of measurements and predictions in the core flow, say from 25 percent to 75 percent span from the hub.

Within the core flow, the Case 3 predictions of the velocities and flow angles at both Stations 7 and 13 generally follow the trends in the benchmark experimental results. However, they are not as good as the predictions obtained in Cases 1 and 2. The maximum disagreement in the flow angle is seen to be less than three degrees and in the

flow velocity, less than ten percent. The code also computed much higher total and static pressures, especially at Station 13. This would be expected perhaps, because of the higher losses resulting from the presence of hub corner stall.

G. OBSERVATIONS

Comparison of the Q3DFLO'81 predictions for Cases 1 and 2 clearly demonstrate the need to include the tangential aerodynamic blockage resulting from the wakes, or an equivalent measure of the departure from axisymmetry, in computing the compressor throughflow. The good agreement of the predictions of Case 2 with the benchmark experimental results, is considered to validate the code's numerical method.

Results from Case 3 also show that it is necessary to know in advance whether the compressor being modelled has an extensive stalled region of flow. If the compressor has an extensive region which is stalled, the subroutines contained in Q3DFLO'81 for calculating the total pressure losses and deviation angles will not give accurate results.

However, in general, given the correct inputs, the simplified throughflow model is able to predict correctly, both the levels and the spanwise distributions of the flow at each station in an axial flow compressor.

IV. APPLICATION TO A MULTI-STAGE COMPRESSOR

A. BACKGROUND

The three-stage, axial flow compressor test rig at the Turbopropulsion Laboratory of the Naval Postgraduate School (NPS) is presently configured for an experimental program to determine the effect of rotor tip clearance on the efficiency and flow behavior in an axial flow machine. Figure 18 shows a radial section of the compressor. It has three repeating stages of symmetrical blading. It also has a row of inlet guide vanes to provide the required pre-rotation to the first stage rotor. The stator provides the same pre-rotation to each following stage. The design, geometry and construction of the compressor are described in references 7 and 8.

Q3DFLO'81 was applied to analyse the machine performance and flow through the test rig. The purpose was to see whether Q3DFLO'81 could be used to support the experimental research activities on the effect of rotor tip clearance. Furthermore, if Q3DFLO'81 was shown to predict the performance of the test rig correctly, then the predicted throughflow solution could be used as input for the blade-to-blade analysis, which is also available in Q3DFLO'81.

The present chapter deals with the application of the throughflow code contained in Q3DFLO'81 to the NPS compressor test rig. In the process, some practical aspects of throughflow modelling using Q3DFLO'81 were uncovered. The configuration of the test rig modelled here consisted of the IGV's and only the second and third stages, since this was the configuration being used in the experimental investigation of the effects of tip clearance change.

B. EXPERIMENTAL SET-UP

Figure 18 also shows the experimental arrangement that was used to measure the overall stage pressure rise of the compressor. The overall static pressure rise was measured using two static pressure taps located on the shroud 1.6 inches ahead of the second stage rotor and two taps at the exit of the third stage stator. Each pair of taps were spaced about 90° apart.

The mass flow rate was calculated from an inlet bellmouth measurement, involving four impact pressure probes and four static pressure taps spaced equally apart, and one thermocouple sensor.

For the purpose of prescribing the inlet conditions for the code, the flow at the inlet to the IGV was measured. The total temperature was assumed to be uniform and the same as for the bellmouth measurement. The spanwise distribution of the total pressure was measured using a nine probe total pressure rake located 0.87 inches downstream of the exit plane of the strut which was 1.75 inches upstream of the IGV. The nine probes were aligned along a radial line positioned almost mid-way between two adjacent struts. The two probes nearest the endwalls were 0.2 inches and 0.25 inches away from the hub and shroud respectively. The static pressure was measured at the shroud and the hub using two static taps, and at mid-channel using a pitot static pressure probe. The velocity was assumed to be axial and its magnitude was calculated from the dynamic pressure distribution.

All measurements were recorded using a Hewlett Packard 3053 Data Acquisition System. A description of the data acquisition system, the instrumentation and the measurement uncertainties are given in reference 9. The uncertainty of pressure rise coefficient and flow coefficient was established from repeated measurements to be 0.5 percent and 0.6 percent respectively.

C. EXPERIMENTAL MEASUREMENTS

Experimental measurements were obtained at a fixed compressor speed for four mass flow rates. For performance mapping, the mass flow rate is expressed in terms of the dimensionless flow coefficient (ϕ) defined as

$$\phi = \frac{\dot{m}}{\rho_{igv} A_{igv} U_m}$$

where \dot{m} is the massflow rate determined from the bellmouth measurement, ρ_{igv} and A_{igv} are the density and annulus area respectively at the IGV inlet, and U_m is the mid-span peripheral speed of the rotor.

The flow coefficients so obtained were 0.61, 0.67, 0.70 and 0.75. Table 1 tabulates the pertinent experimental measurements and calculated parameters. The static pressure rise (ΔP_s) across the rotors and stators is expressed by the dimensionless quantity, Π_s , which is defined as

$$\Pi_s = \frac{\Delta P_s}{\frac{1}{2} \rho_{igv} U_m^2}$$

The variation of Π_c with ϕ is the compressor 'characteristic'. In the following section, the measured characteristic is compared with the Q3DFLO'81 code prediction.

Table 1. EXPERIMENTAL FLOW AND PRESSURE COEFFICIENTS

ϕ	0.612	0.670	0.701	0.748
Π_c	1.050	0.952	0.887	0.799
$T_{bell} (^{\circ}R)$	534.56	533.55	534.21	534.88
P_{OT} (inw)	409.56	409.51	409.49	409.46
P_{OS} (inw)	407.53	407.06	406.79	406.37
ρ_{bell} (lbm ft ³)	0.074223	0.074278	0.074137	0.073967
V_{bell} (ft sec)	95.50	104.88	110.21	118.03
d_{bell} (ins)	36.0	36.0	36.0	36.0
A_{bell} (ft ²)	7.0686	7.0686	7.0686	7.0686
\dot{m} (lbm sec)	50.104	55.066	57.753	61.712
T_{ig} ($^{\circ}R$)	533.56	532.55	533.21	533.88
$P_{s,ig}$ (inw)	392.91	393.50	393.83	394.40
ρ_{ig} (lbm ft ³)	0.071748	0.071992	0.071963	0.071978
P_{is} (inw)	392.58	393.11	393.35	393.87
P_e (inw)	407.00	406.24	405.59	404.88
ΔP_i (inw)	14.42	13.13	12.24	11.01
N (rpm)	1609.6	1609.6	1610.6	1610.8
R_m (ft)	1.20	1.20	1.20	1.20
U_m (ft sec)	202.27	202.27	202.39	202.42

The measured spanwise distributions of total and static pressure and the velocity calculated from them, are shown in Figure 19. The static pressure is observed to be skewed linearly from hub to shroud based on the shroud, mid-span and hub measurements. The (axial) velocity was calculated from the measurements using

$$V_x = \frac{\sqrt{2(P_{t,igv} - P_{s,igv})}}{\rho_{igv}}$$

where the density (ρ_{igv}) in pounds mass per cubic foot at the IGV inlet was obtained using

$$\rho_{igv} = \frac{P_{s,igv}}{T_{s,igv}} \times \frac{518.69}{408.2} \times 0.07647$$

D. MODELLING OF THE COMPRESSOR

The NPS 3-stage axial compressor has a cylindrical annulus. The radius of the hub and tip are 10.8 inches and 18 inches respectively. The airfoils of the rotor and stator are both of the C series type with a modified thickness distribution. The compressor was modelled from the measurement plane upstream of the IGV to the station downstream of the third stage stator. Figure 20 shows the computational mesh, which had a total of 25 stations and 10 axial grid lines. Grid lines were clustered towards the shroud by specifying a repartition factor of 0.1. As the total number of nodes then exceeded the maximum of 600 nodes allowed in the Q3DFLO'81 code, the analysis was done in two parts. The first part analysed the flow from Station 1, ahead of the IGV, to a station immediately downstream of the third stage rotor. The prediction at this station was then used as input to a second calculation from the inlet of the third stage stator to the measurement station downstream of the stator exit.

The input data required by the code for the inlet condition at Station 1 were the mass flow rate, the spanwise distributions of the velocity components, the total temperature and the total pressure.

E. EFFECT OF THE STRUT WAKES

The boundary layer displacement thickness at the shroud was measured to be about 0.13 inches in a separate study by Tarigan [Ref. 10]. For the code prediction, a nominal endwall blockage of 2.6 percent was specified at Station 1, which is equivalent (in area) to a 0.15 inches displacement thickness at the shroud. The higher blockage factor was to account for the thicker boundary layer at the junction of the strut and the endwalls and the negligibly thin boundary layer at the hub.

A disagreement with the mass flow measurement obtained from the inlet bellmouth was noted when the spanwise velocity distribution at the IGV inlet was integrated to determine the mass flow rate. The data in Table 2 show that the massflow rates determined from the measurements at Station 1 were about 3.5 percent higher than the bellmouth measurement for all four flow coefficients.

Table 2. BELLMOUTH VS INLET RAKE MEASUREMENTS OF FLOW RATE

ϕ	0.612	0.670	0.701	0.748
Π_s	1.050	0.952	0.887	0.799
m_{bell} (lbm sec)	49.962	55.066	57.750	61.710
m_{gv} (lbm sec)	51.737	57.004	59.781	63.758

Examination revealed that the measurement plane at Station 1 was about 21 percent of chord behind the strut trailing edge. There were a total of six struts equally spaced. Figure 21 shows the profile of the strut which had a chord of 4.12 inches and maximum thickness of 0.813 inches. It was known that strut wakes were present at the measurement plane, although they did not intercept the rake sensors. The thickness of the wake had not been measured since the mechanical arrangement of the casing did not permit a circumferential survey of the flow. However, two static pressure taps on the shroud, located between the IGV outlet and the 2nd stage rotor inlet, did indicate an increase in the static pressure, as the flow proceeded downstream. This could be explained by the diffusion of the strut wakes in the annulus. The presence of the strut wakes also explains the apparent increase in mass flow rate indicated by the rake at Station 1. The strut wakes, were effectively a two dimensional blockage, causing a reduction in the circumferential flow area and an increase in the local flow velocity from hub to shroud at the IGV measurement plane.

F. ADAPTATION OF THE INLET FLOW CONDITION

The displacement thickness of the strut wakes could be expected to be fairly uniform in the core of the flow but not at the corners between the strut and the endwalls. For numerical modelling, it was reasonable to assume that it was uniform from hub to shroud. The endwall boundary layer displacement thickness, the mass flow rate determined from the bellmouth measurement and the spanwise axial velocity measured at Station 1 were sufficient to calculate a unique displacement thickness of the strut wake which gave the measured mass flow rate.

The wake displacement thickness can be viewed as tangential blockage. Unfortunately, the Q3DFLO'81 code was unable to accept a tangential blockage factor as input data. Consequently, it was assumed that the strut wakes were completely diffused at constant radii before entering the IGV, and this diffusion process was

calculated externally from the Q3DFLO'81 code. Appendix (B) describes the diffusion calculation for the strut wakes. The spanwise distributions of the diffused (or 'mixed out') axial velocity and total pressure were then used as boundary conditions for the code, at Station 1.

One could expect that, by assuming the wakes had diffused before entering the IGV, instead of letting them be swallowed by the IGV's and then diffused gradually to have negligible thickness at Station 8, the prediction of the axial velocity component would differ from the actual value immediately downstream of the IGV. But at Station 8, and beyond where it was expected that the strut wakes would have diffused completely, the code prediction would be valid. A comparison of the code predictions with the experimental measurements for the static pressure at the shroud at Station 8 would give a good indication of the validity of the above reasoning.

G. RESULTS FOR THE ADAPTED INLET FLOW

The endwall blockage and wake thickness of each strut at Station 1 required for the code calculation to match the measured static pressure at Station 8, are shown in Table 3.

Table 3. DISPLACEMENT AND WAKE THICKNESSES AT STATION 1

Flow Coefficient	0.612	0.670	0.701	0.748
Endwall Blockage @ Stn 1 (%)	2.6	2.6	2.6	2.6
Wake Thickness (inch)	0.513	0.528	0.528	0.413
Computed P_r @ Stn 8 (inw)	392.66	393.10	393.44	393.80
Measured P_r @ Stn 8 (inw)	392.58	393.10	393.35	393.87

It was found that a wake displacement thickness of 0.528 inches and an endwall blockage factor of 0.976 produced a match with the measured static pressure at Station 8 fairly well. The ratio of the wake displacement thickness to the strut maximum thickness was 0.59.

Figure 22 shows the spanwise distributions of total and static pressures and axial velocity after the diffusion. It can be seen that the total pressure was hardly affected. As expected, there was an appreciable increase in the static pressure of about 0.5 inches of water due to a 3.5 percent reduction in velocity.

H. COMPARISON OF THE OVERALL PERFORMANCE

Q3DFLO'81 was used to predict the overall performance at each of the four flow coefficients both with and without strut wake diffusion at Station 1. The computed variation of Π , vs ϕ is shown in Figure 23 denoted as follows:

- Case 1: Experimental Measurement.
- Case 2: Q3DFLO'81 Prediction with Correction for Strut Wake Blockage.
- Case 3: Q3DFLO'81 Prediction without Correction for Strut Wake Blockage.
- Case 4: Meanline Analysis [Ref. 9]

It should be noted that the flow coefficient of Case 3 was based on the actual mass flow rate rather than the apparently higher mass flow rate measured at the IGV inlet.

Comparing Cases 2 and 3, Case 2 shows significantly higher pressure rise coefficients than does Case 3. This is probably for two reasons. First, the reduced axial velocity which results from wake diffusion causes an increase in the blade loading. The IGV exit flow angle calculated by the code is independent of the value of the flow coefficient. The code predicted essentially the same absolute flow angles at all stations from the exit of the IGV at Station 4 to the inlet of the first rotor at Station 9, both for Cases 2 and 3. With the same absolute flow angle, and lower axial velocity, Case 2 involves a correspondingly lower absolute tangential velocity upstream of the rotor. This would cause an increase in the relative tangential velocity component, which results in an increase in the blade loading of the first rotor. Second, the total pressure loss coefficient calculated by the Q3DFLO'81 subroutine for Case 2 was significantly lower than for Case 3 for all blade rows. This suggested that Case 2 involved more favorable incidence angles than Case 3.

Comparing Case 2 with Cases 1 and 4, Case 2 showed better agreement with Case 1 (measurements) at the flow coefficient of 0.612 but departed by an increasing margin for flow coefficient above 0.67. Since the design flow coefficient was about 0.64, the prediction was better near the design condition than at off-design conditions, which might be expected.

I. EFFECT OF THE IGV EXIT FLOW UNDERTURNING

It was suspected that the difference in the pressure rise coefficient between the experimental measurements and the predictions at all conditions might be the result of underturning of the IGV exit flow, which had been observed in the compressor.

Waddell [Ref. 11] had measured the IGV exit flow angle and had established that it was independent of the flow coefficient. He showed that the turning angle was smaller than the design intent over a large part of the span. The Q3DFLO'81 prediction of the IGV exit flow angle for Case 2 is compared with Waddell's measurement in Figure 24. It can be seen that the flow was underturned over 70 percent of the span and the maximum underturning was about five degrees.

Since the metal trailing edge angle of the IGV could be adjusted readily in Q3DFLO'81, attempts were made to simulate the measured IGV exit flow angle in Case 2 by adjusting the IGV metal angle. This case is denoted as

- Case 5: Case 2 with Simulated Measured IGV Exit Flow Angle

Cases 1 and 2 are shown replotted in Figure 25 with the prediction for Case 5. Case 5 shows a fairly constant improvement over the measured range of flow coefficients. It reduces the difference between prediction and measurement of the pressure rise coefficient by about 40 percent at the on-design flow coefficient but has progressively less effect for higher flow coefficients.

J. OBSERVATIONS

From the above studies, it is clear that it is desirable to have provision for introducing tangential aerodynamic blockage as input data. The presence of the struts ahead of the IGV is typical for an axial flow compressor. Its effect on the flow velocity at the inlet of the IGV must be considered, and this can be accounted for by using the tangential aerodynamic blockage factor.

The prediction of the performance near the design condition is much better than at off-design conditions. An accurate description of the flow conditions at the inlet of the compressor is essential if the code is to give good predictions at following stations.

The prediction of the IGV exit flow angles by Q3DFLO'81 differed from the measured values. As a result, the predicted flow downstream of the IGV exit was not representative of the physical flow. It is noted that the code does not contain a separate correlation for deviation angle from IGV's, but treats the IGV's as a stator (compressor) blade row.

V. THE INVISCID BLADE-TO-BLADE SOLUTION

A. BACKGROUND

Q3DFLO'81 has a separate inviscid code to solve for the velocity and pressure fields on the axisymmetric streamsurface between two adjacent blades. The blade-to-blade code requires the inlet and outlet flow conditions to be specified. The code can be run independently by entering the inlet and outlet conditions manually. Alternatively, Q3DFLO'81 can optionally couple the throughflow code with the blade-to-blade code. In this case, Q3DFLO'81 would first compute the results for the throughflow. It then transfers the necessary data internally to the blade-to-blade code, for the specified blade row, and continues with the blade-to-blade computation.

The blade-to-blade code was applied to Cases 2 and 5 (of the preceding chapter) for flow coefficients of 0.61 and 0.67 and the inviscid blade-to-blade solution for the second rotor at the tip section was generated.

B. INPUT DATA AND SOLUTION

The blade profile and the computational mesh for the rotor tip calculation are shown in Figure 26 and Figure 27 respectively. A total of 25 stations was used. Stations 6 and 20 are the inlet and outlet stations of the rotor blade passage. There are two options for specifying the outlet flow condition. Either the Kutta condition is imposed at the trailing edge or the exit relative flow angle must be specified. The solution presented herein is based on the use of the Kutta condition.

As an example of the blade-to-blade computation, the results are presented here for Case 5 at a flow coefficient of 0.61. The computed iso-pressure lines on the axisymmetric stream surface at the tip and the pressure coefficients on the suction and pressure sides of the blade, are shown in Figure 28 and Figure 29 respectively.

VI. CONCLUSIONS AND RECOMMENDATIONS

The finite element code Q3DFLO'81 was applied successfully to two different axial compressor geometries. First, application to a 'benchmark' compressor, for which very complete flow survey data were available, showed the importance of accounting for peripherally non-uniform flow (blockage) effects. Second, application to the NPS axial research compressor demonstrated clearly the difficulties that are inherent in comparing code predictions with experimental data when the experimental information is not fully comprehensive, and when the measured flow is not valid as an inlet boundary condition for the code.

In spite of the complex nature of the flow within the NPS compressor test rig, when a valid inlet boundary condition was derived from the measured data, the throughflow code of Q3DFLO'81 predicted the pressure rise fairly well near the design operating condition. An analysis of the measurements, in order to derive a proper boundary condition for the code, was required in order to achieve agreement. At off-design conditions, the code was not as successful. For flow near to the design condition, the inviscid blade-to-blade code was used successfully to generate the iso-pressure lines and the blade surface pressure distributions for the tip section of the second rotor.

From the above experience, the following were found to constrain the application of Q3DFLO'81:

- The code does not accept a tangential aerodynamic blockage factor as an input for the throughflow prediction. This did not allow the strut wakes at the IGV inlet measurement plane to be introduced to the throughflow in the manner that they occurred physically.
- The code allots the endwall blockage factor at the inlet station equally between the hub and the case walls. This was not representative of the flow in the compressor test rig. The blockage at the inlet was largely due to the boundary layer displacement thickness at the case wall. The hub had a negligibly thin boundary layer.
- The code only permits the meridional mesh lines to be clustered either towards the case wall or the hub. In applying Q3DFLO'81 to the benchmark data set and the compressor test rig, it was found that it would be desirable if the meridional mesh lines could be clustered towards both the case wall and the hub. This is because abrupt changes in the flow conditions tend to occur at both the case wall and the hub.
- The code limits the capacity of the mesh to 600 nodes and the input values for each variable such as the total pressure at the inlet station to 10 points. A larger

capacity is required to model a multi-stage geometry using grid lines clustered near the walls.

- The use of two dimensional cascade data for calculating losses across the rotor and stator blade rows was shown not to be accurate for a blade row with corner stall. It is therefore advisable to establish whether stall regions are present in any new compressor to which the code is applied.
- The code did not predict the exit flow angle of the inlet guide vane correctly. Although this was overcome by adjusting the geometry of the inlet guide vane in the code, the correction required that the actual flow angle be known. This information would not generally be available in a normal application of the code.

The use of the code in the tip-clearance investigation on the NPS compressor is seen to be limited by the above constraints, but also by constraints on the experiment itself. For example, the spanwise distribution of the strut wake profile at the inlet measurement plane needs to be measured accurately. Although the assumptions of uniform wake thickness and wake diffusion on the constant radii axisymmetric stream surface worked fairly well, an accurate representation of the inlet velocity near the case wall is required to obtain an accurate prediction of the pressure rise, and a more precise inviscid solution at the rotor tip.

Unfortunately, the compressor is not in general, equipped for peripheral flow surveys, and the required modification to the heavy case wall would be difficult and expensive to make. It is clear however, that peripheral survey data and the means to input such data into the code, are essential.

Finally, it is noted that the present assessment was made using an early edition of the code. Later versions of the code might be less constrained.

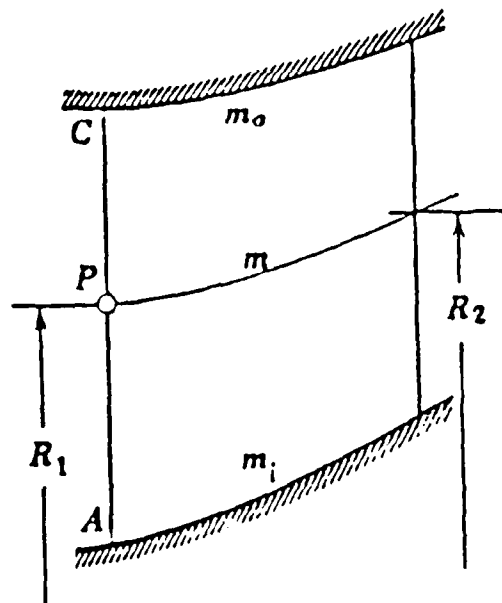
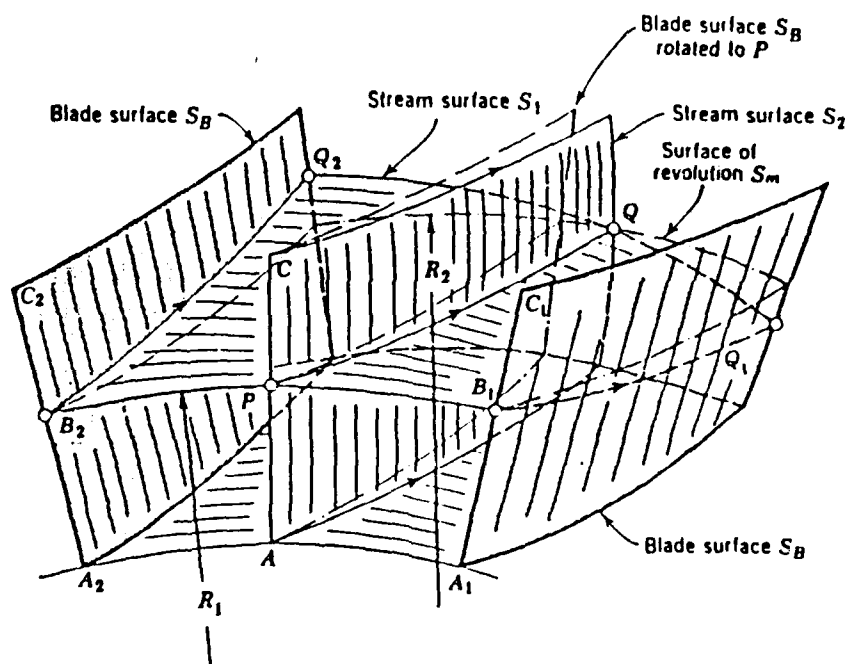


Figure 1. Stream Surfaces Through an Annular Blade Row

Source: Varva M. H., *Aerothermodynamics and Flow in Turbomachines*, Wiley, New York, May 1974.

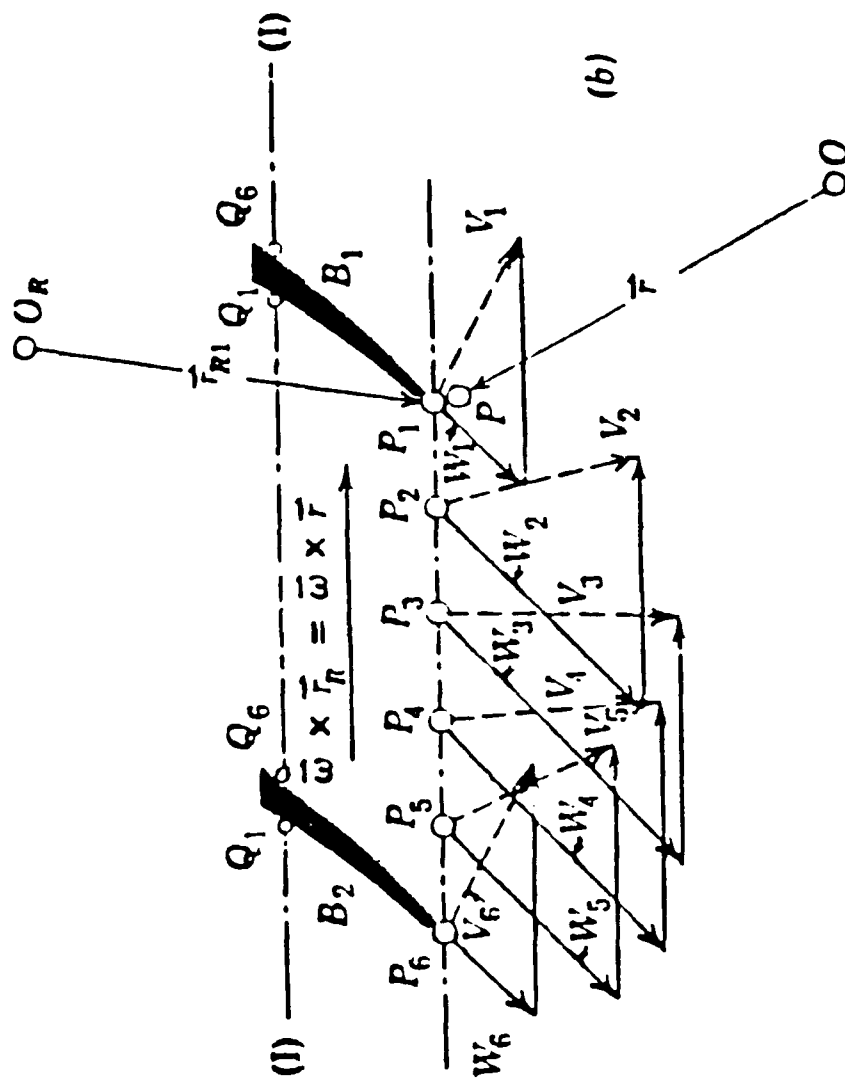


Figure 2. Velocities from a Rotating Row of Blades

Source: Varva M. H., *Aerothermodynamics and Flow in Turbomachines*, Wiley, New York, May 1974.

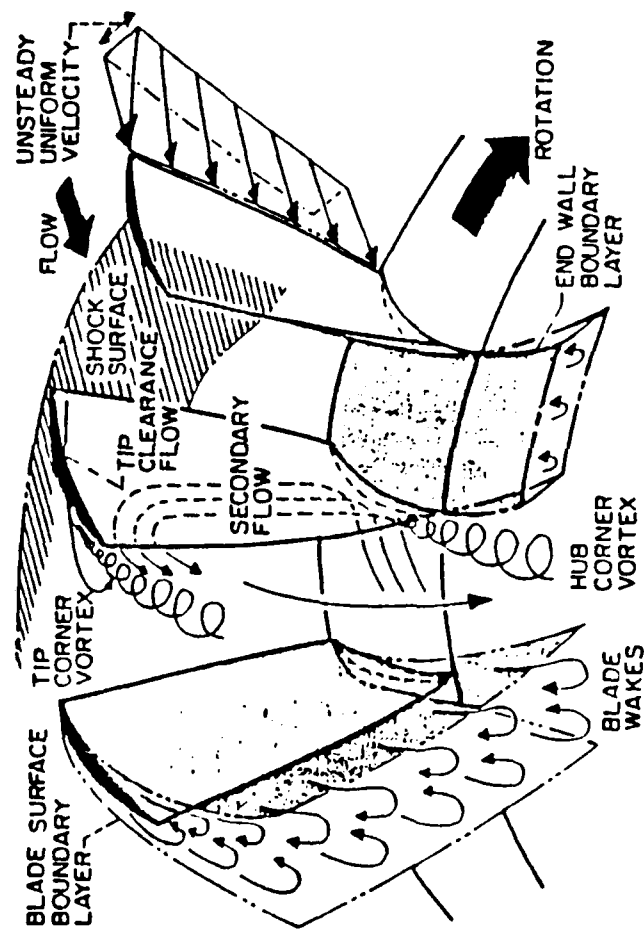


Figure 3. Complex Flow Phenomena in a Compressor Rotor

Source: Naval Postgraduate School Report NPS67-84-022, *Computational Models for Turbomachinery Flows*, by Hirsch, C., Dec 1984.

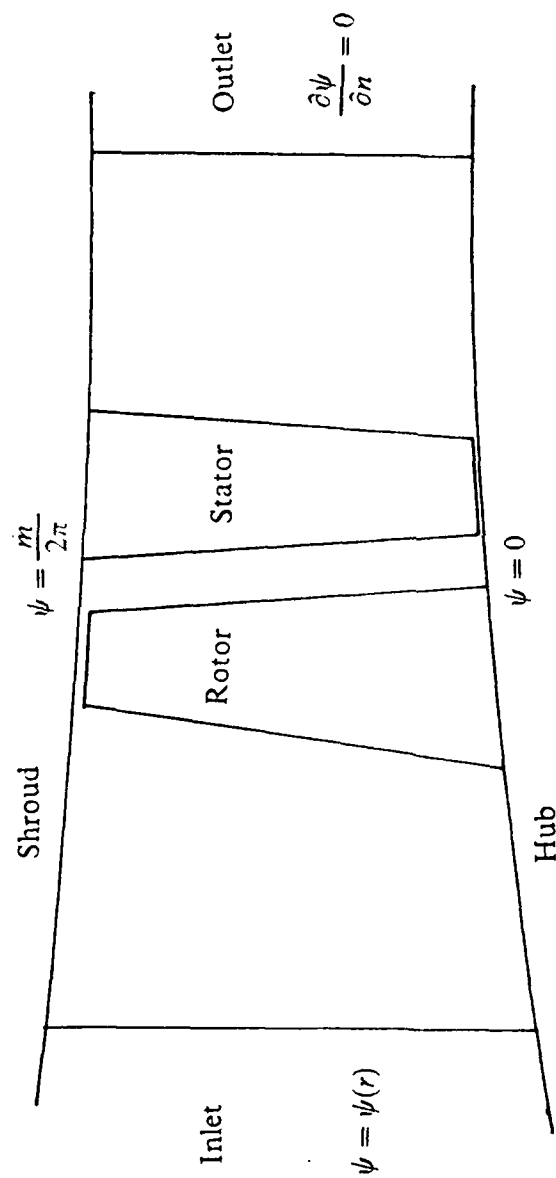


Figure 4. Schematic Meridional Section of a Compressor Stage

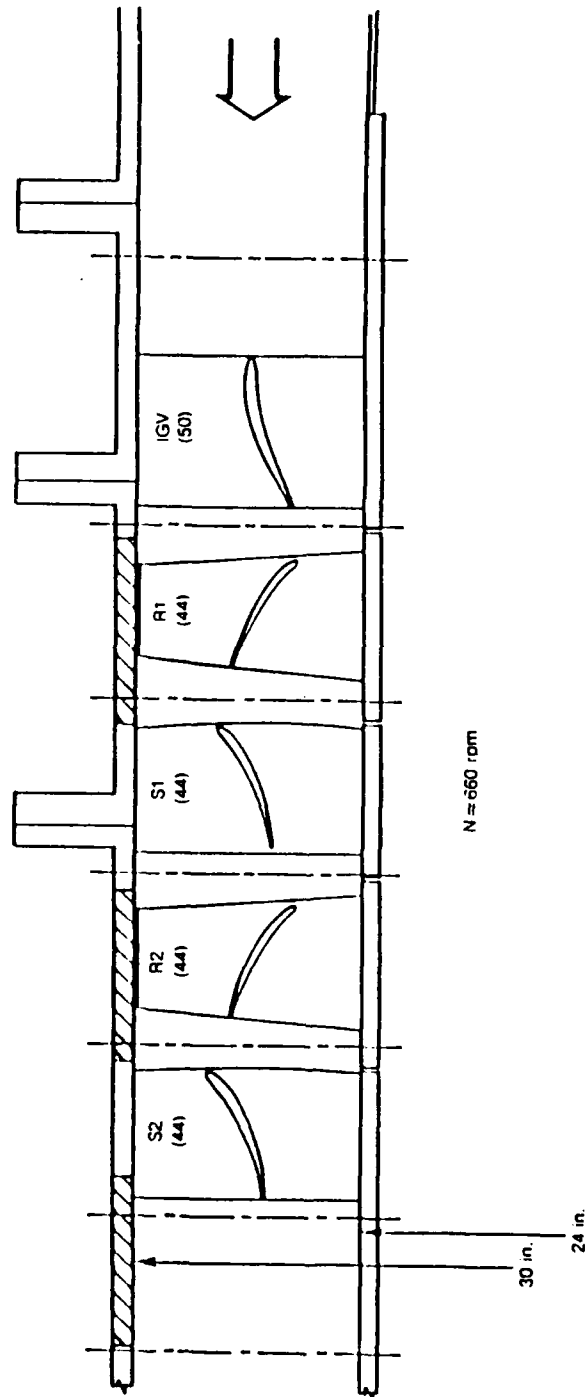


Figure 5. Geometry of the Benchmark Compressor

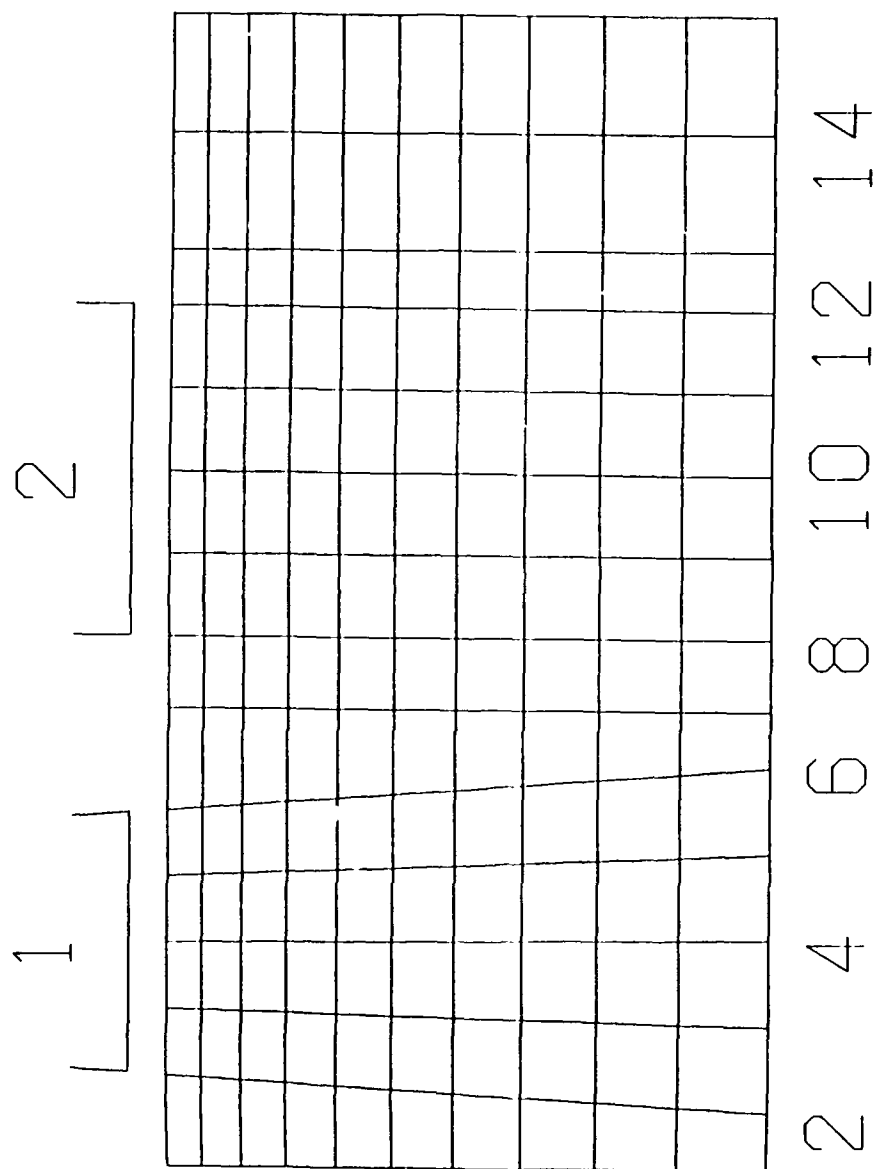
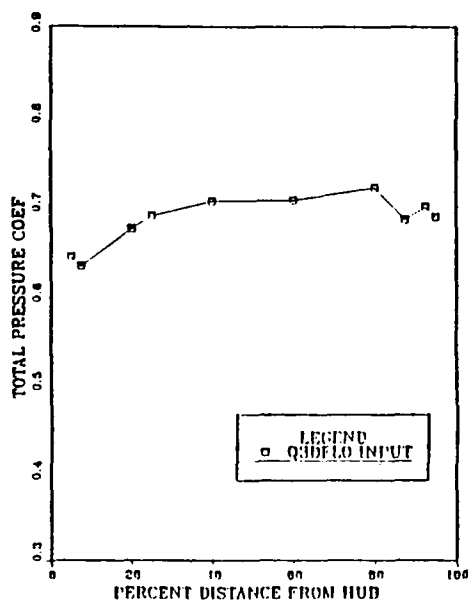
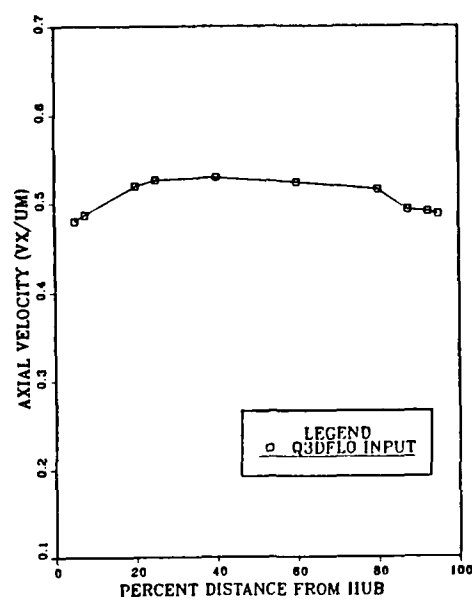


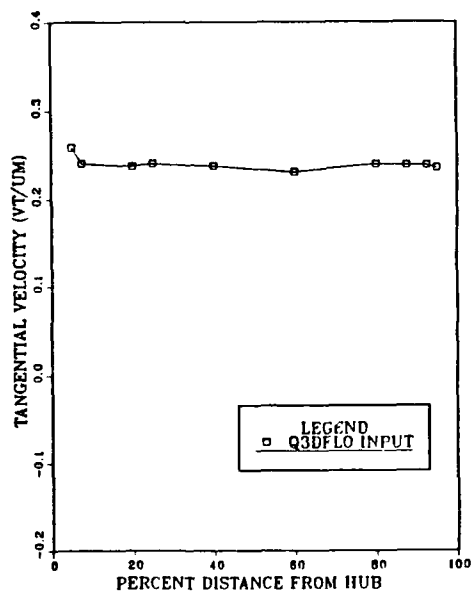
Figure 6. Computational Mesh for the Benchmark Compressor



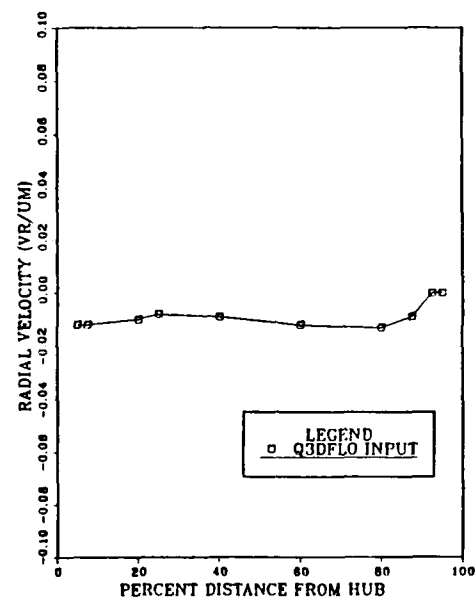
(A)



(B)

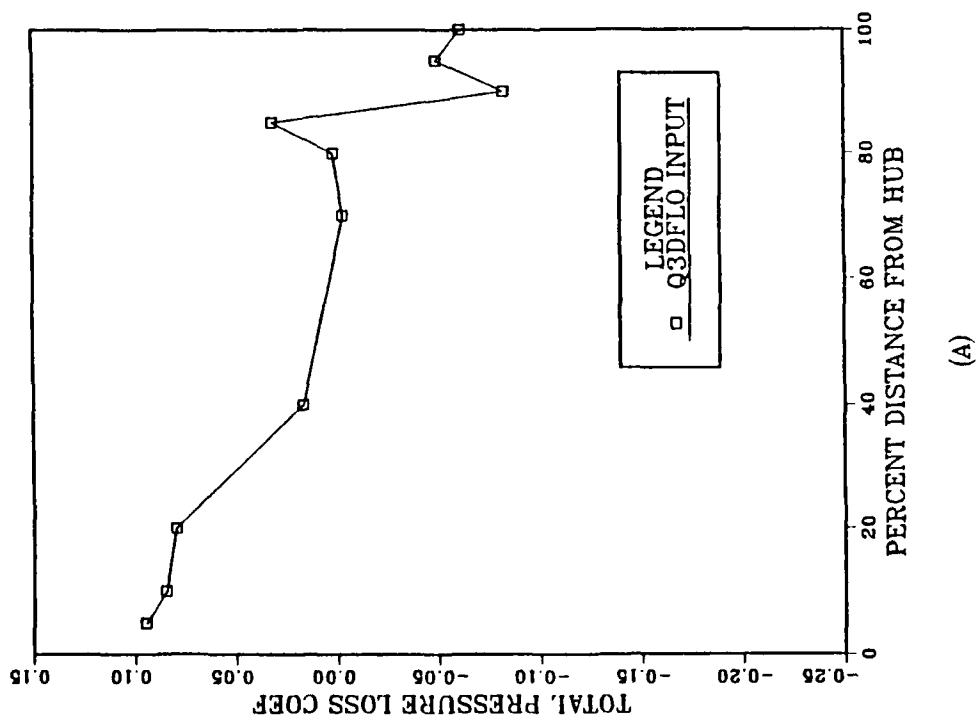


(C)

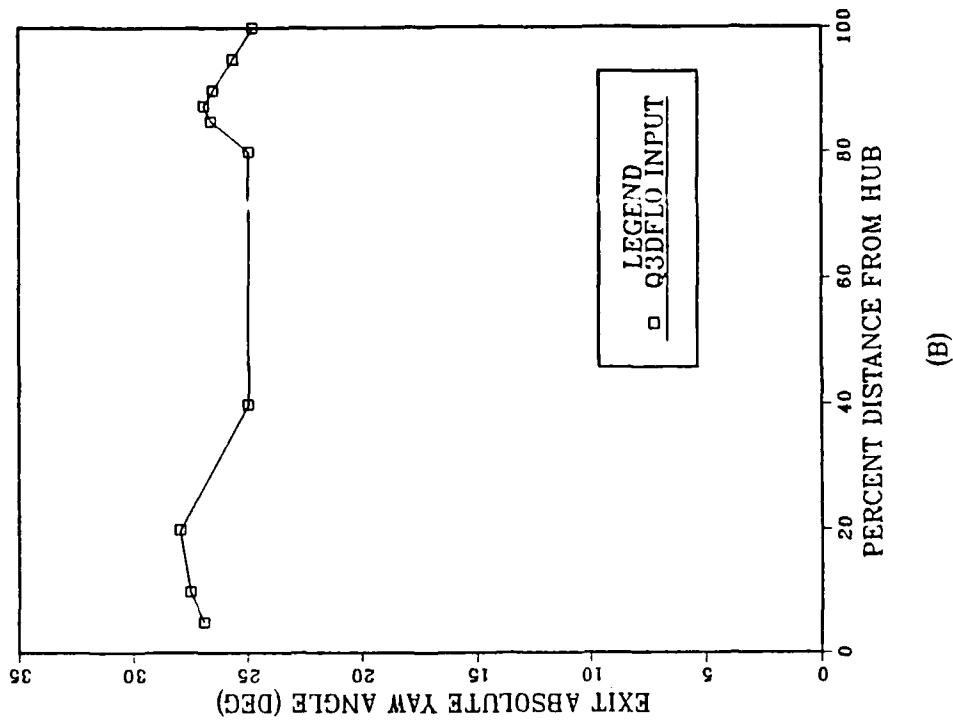


(D)

Figure 7. Spanwise Distribution of the Flow Properties at Station 1



(A)



(B)

Figure 8. Spanwise Distribution of the Loss Coefficient and Exit Flow Angle for the Second Rotor

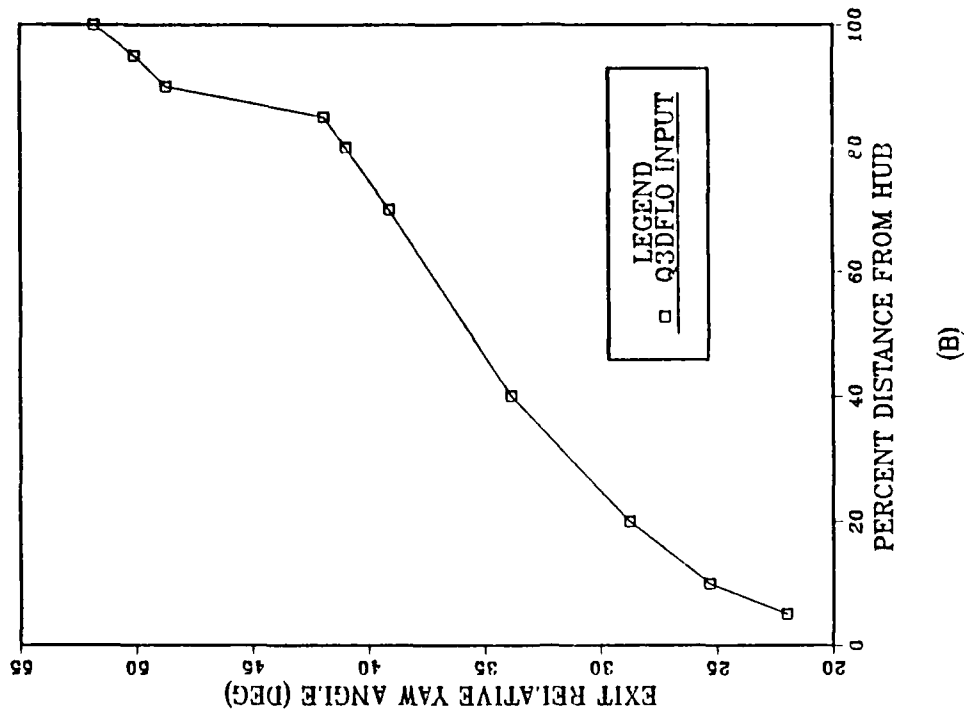
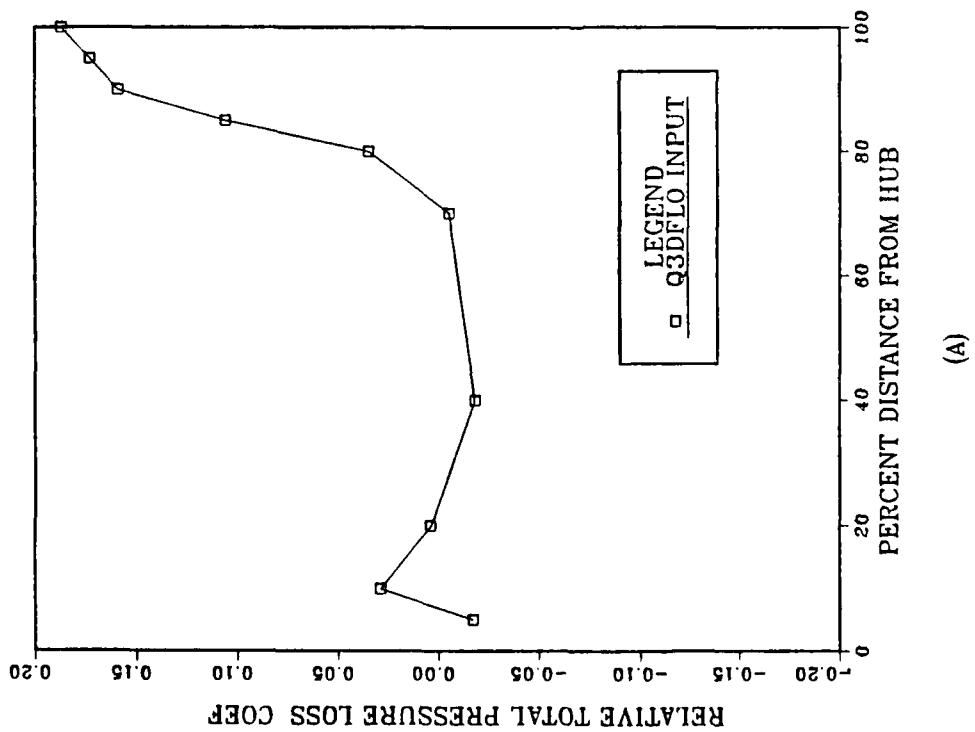
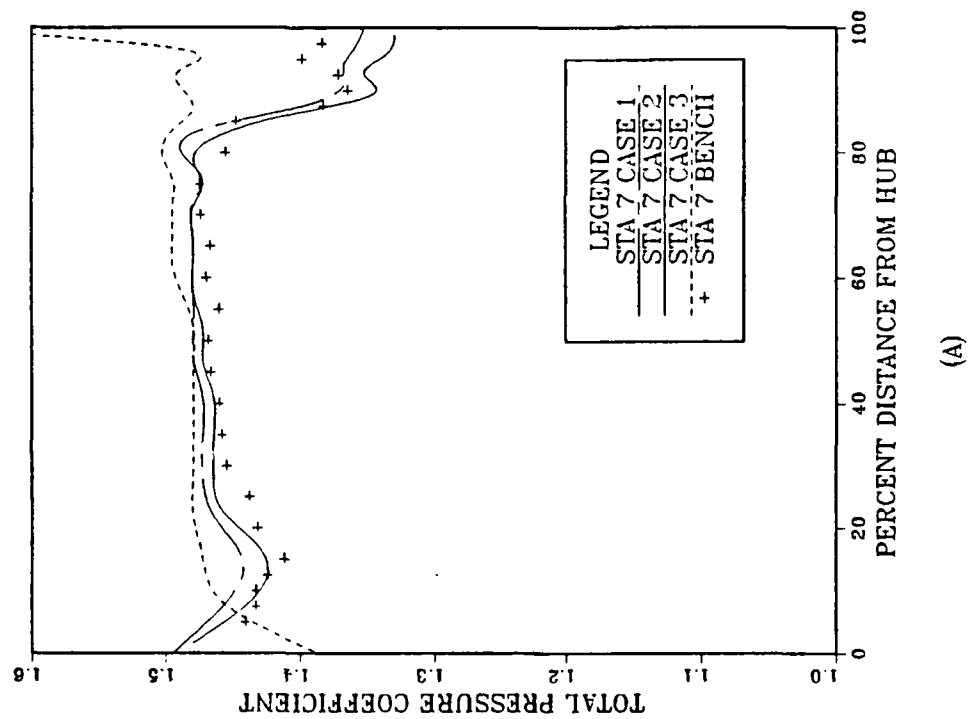
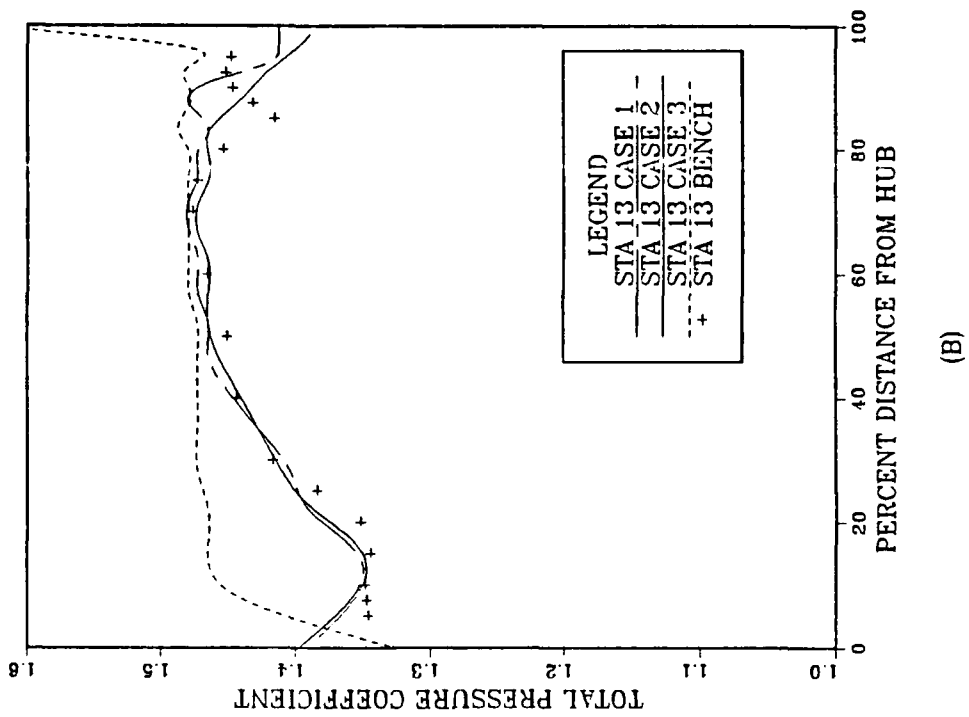


Figure 9. Spanwise Distribution of the Loss Coefficient and Exit Flow Angle for the Second Stator

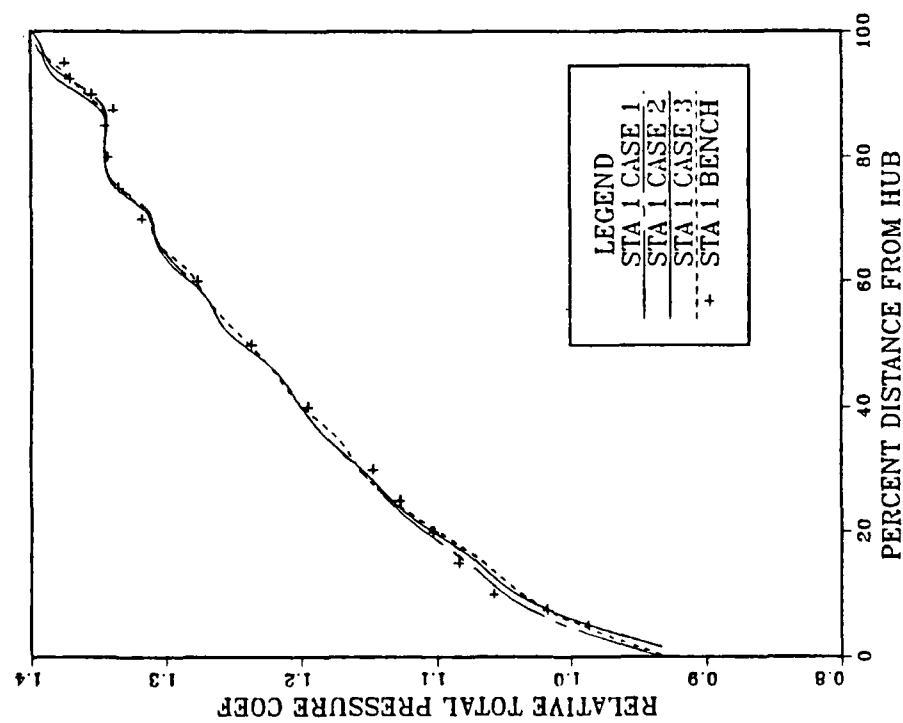


(A)

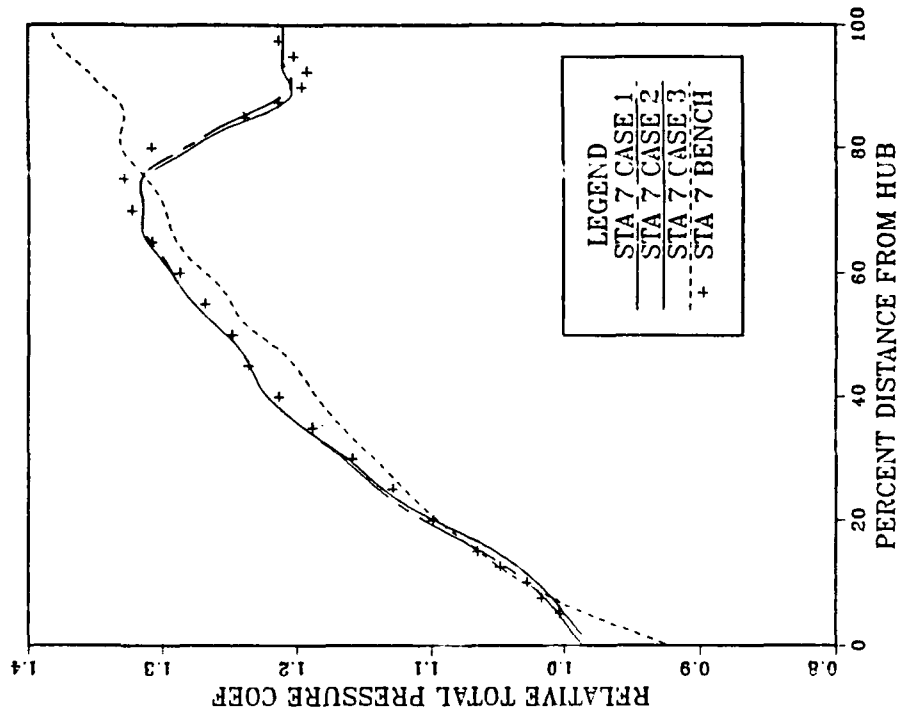


(B)

Figure 10. Spanwise Distribution of the Total Pressure Coefficient at Stations 7 and 13



(A)



(B)

Figure 11. Spanwise Distribution of the Relative Total Pressure Coefficient at Stations 1 and 7

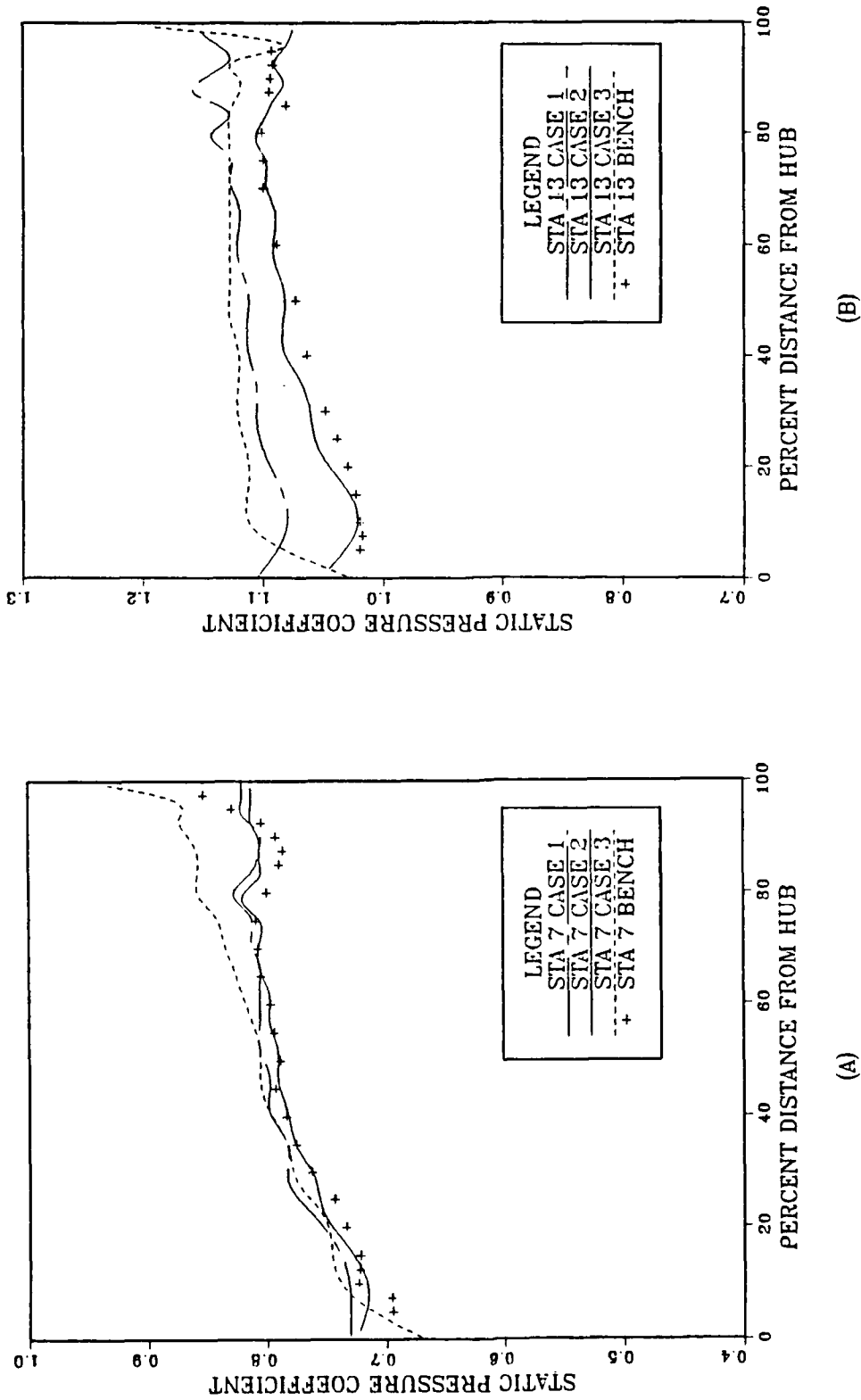
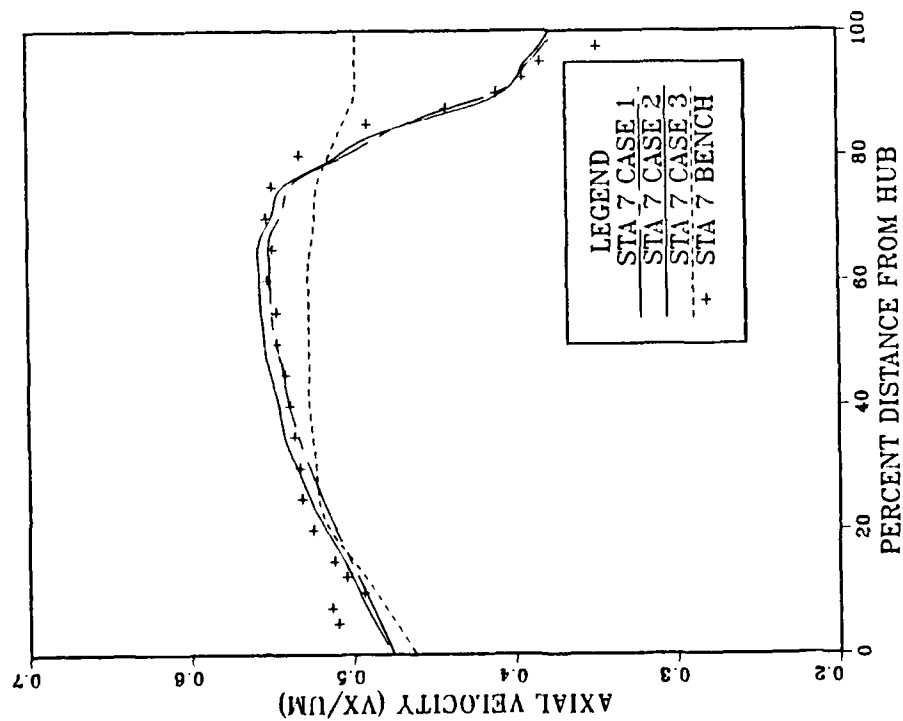
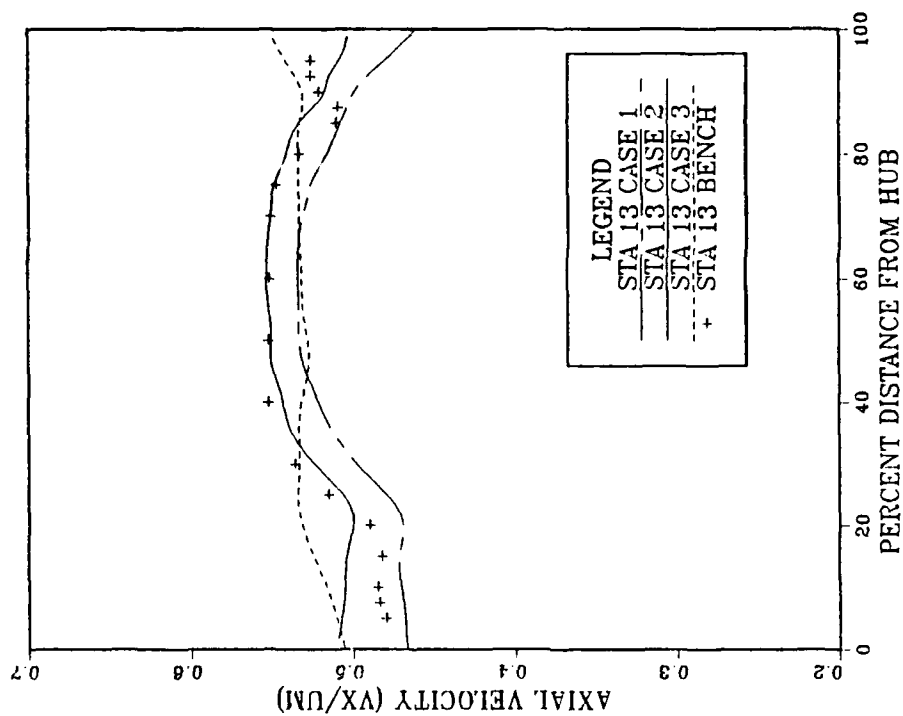


Figure 12. Spanwise Distribution of the Static Pressure Coefficient at Stations 7 and 13

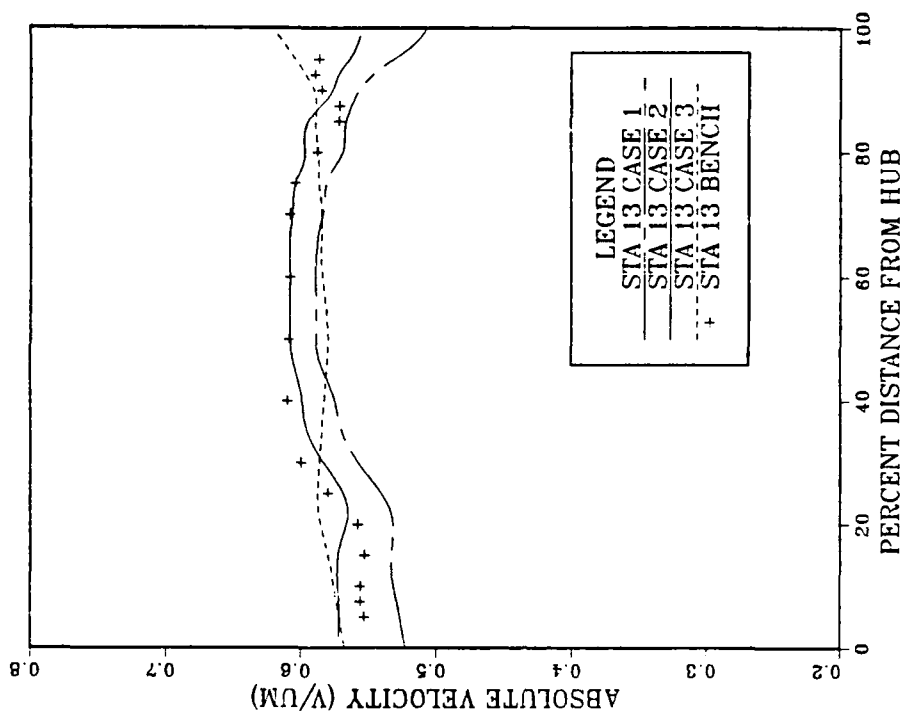


(A)

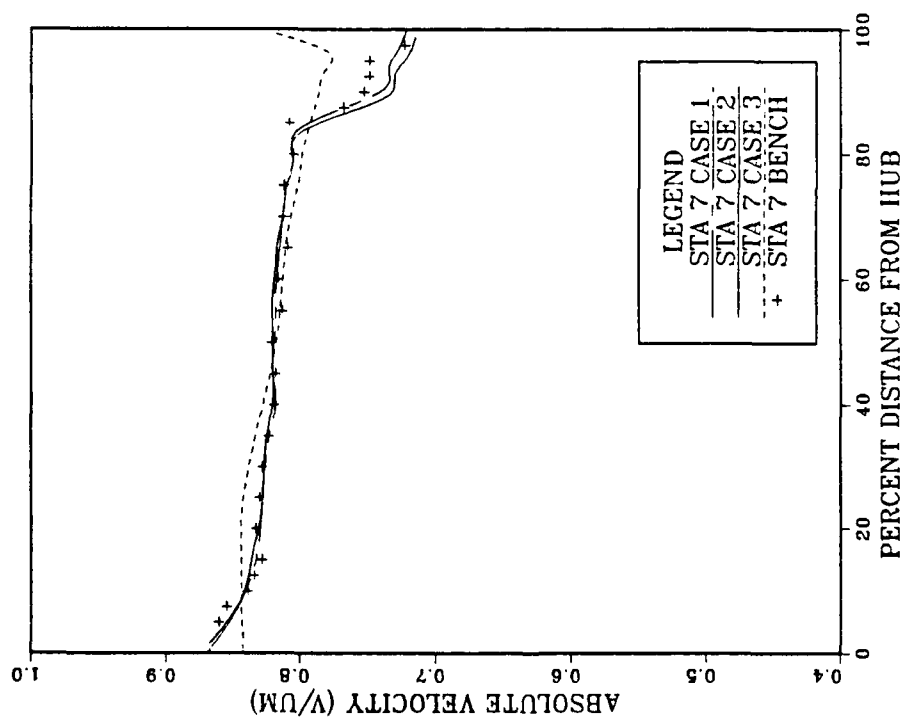


(B)

Figure 13. Spanwise Distribution of the Axial Velocity Component at Stations 7 and 13

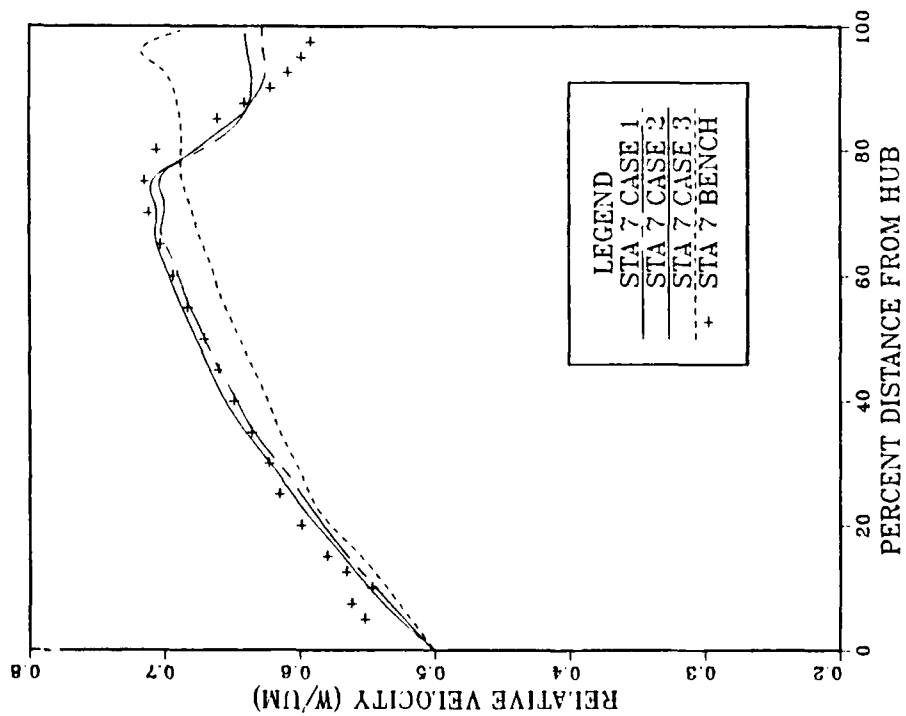


(A)

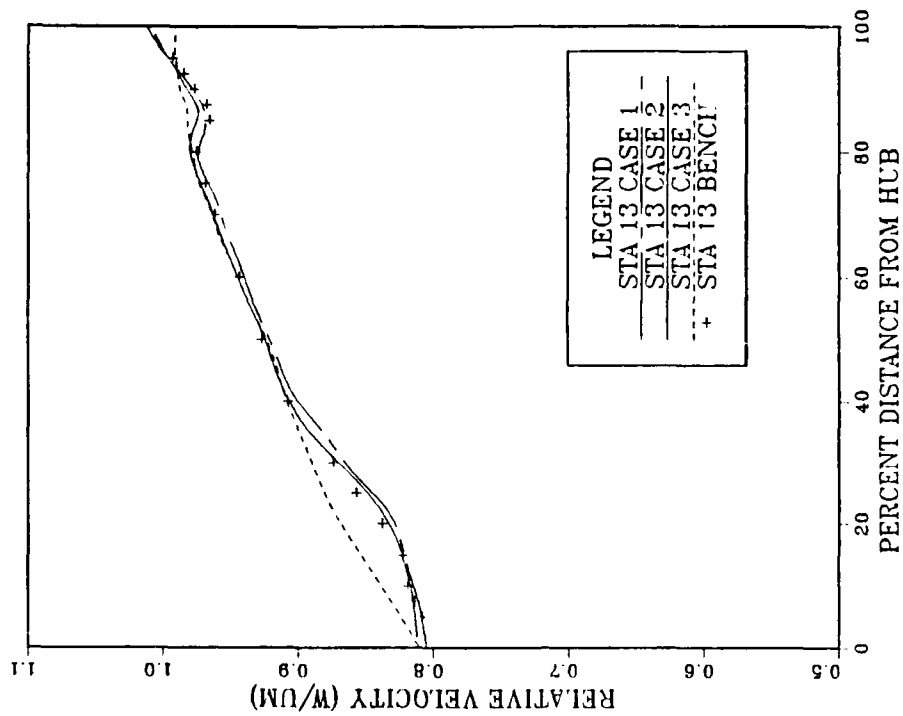


(B)

Figure 14. Spanwise Distribution of the Absolute Flow Velocity at Stations 7 and 13

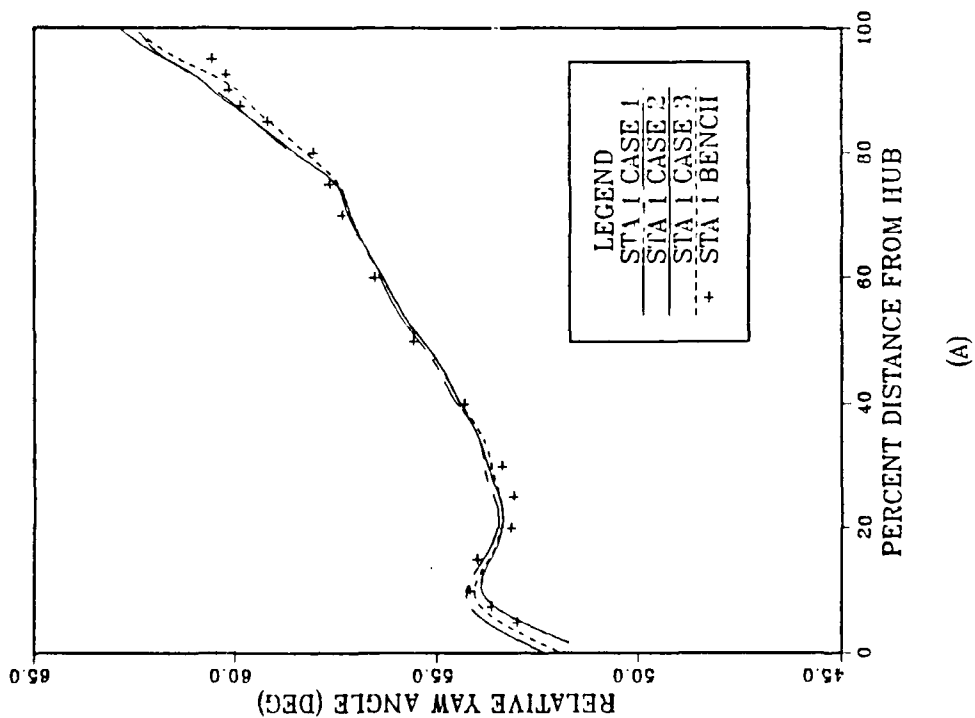


(A)

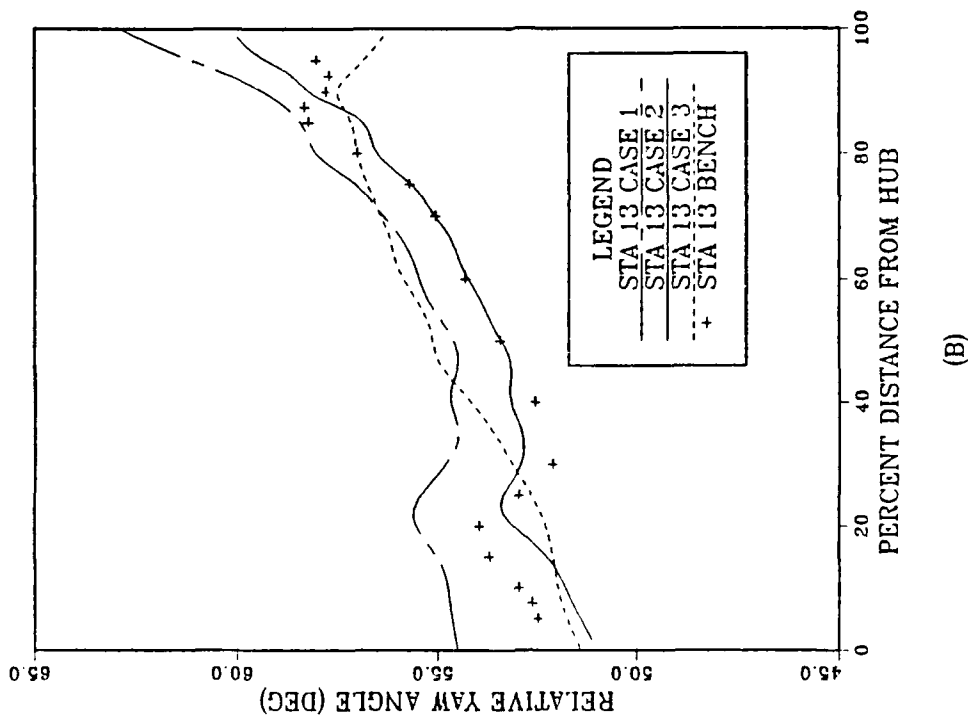


(B)

Figure 15. Spanwise Distribution of the Relative Flow Velocity at Stations 7 and 13



(A)



(B)

Figure 16. Spanwise Distribution of the Relative Flow Yaw Angle at Stations 1 and 13

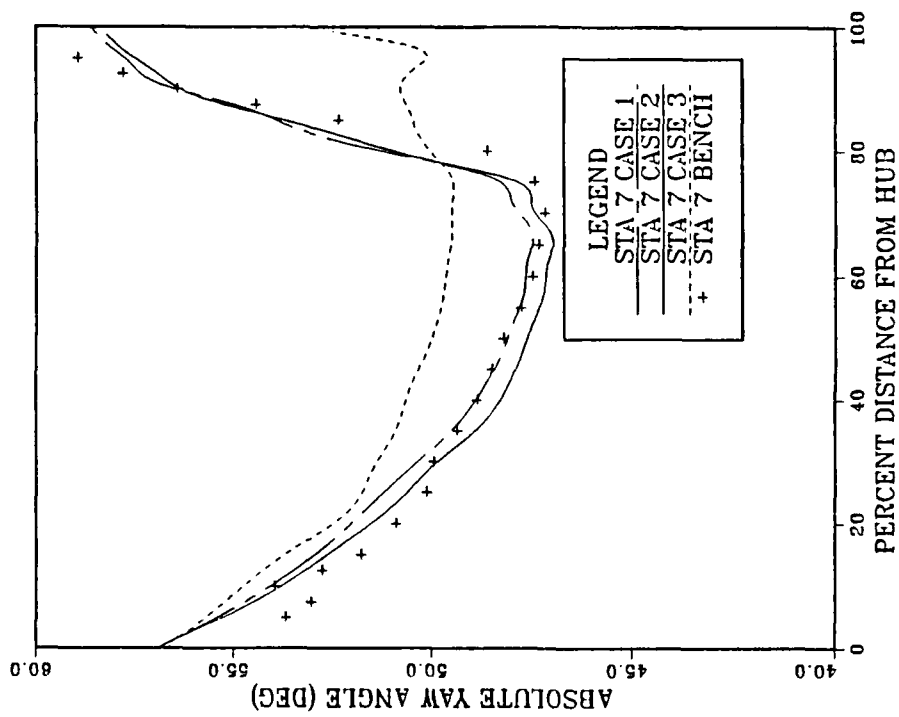


Figure 17. Spanwise Distribution of the Absolute Flow Yaw Angle at Station 7

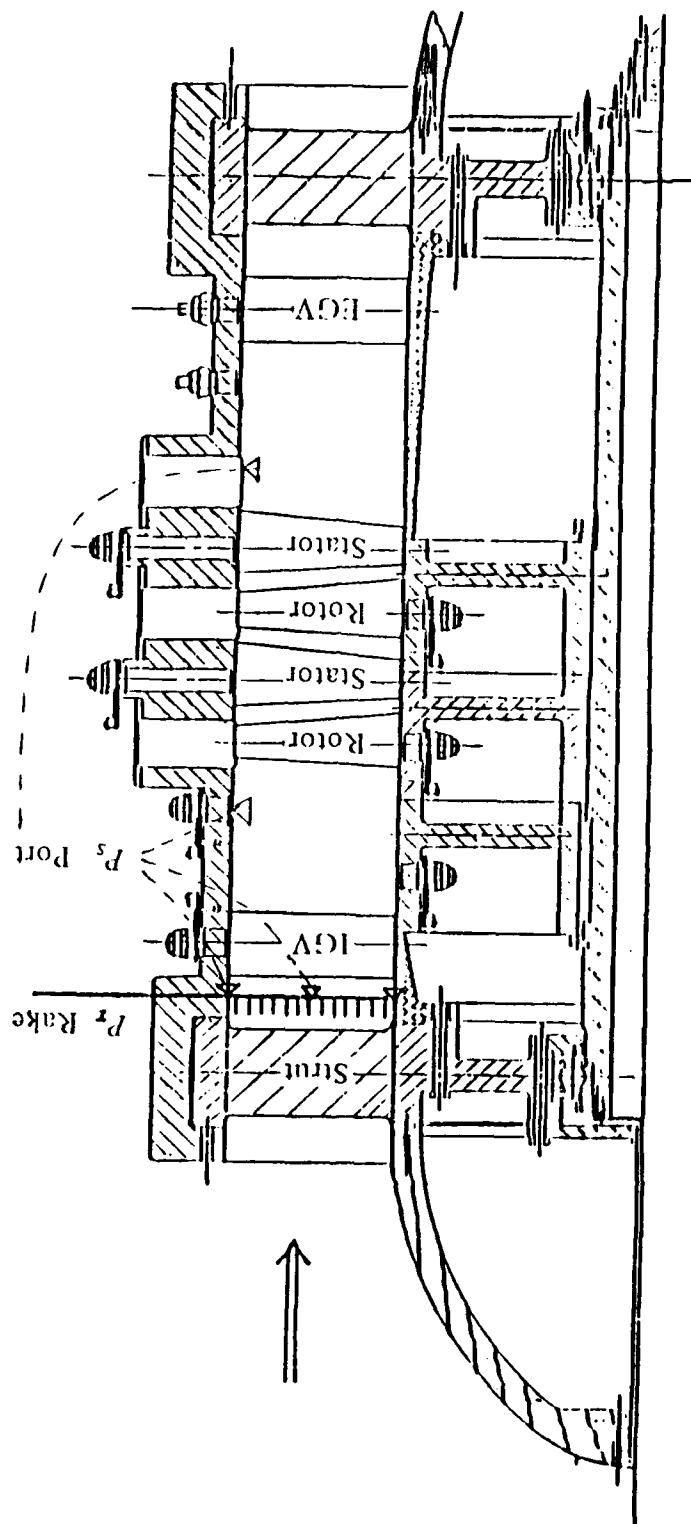
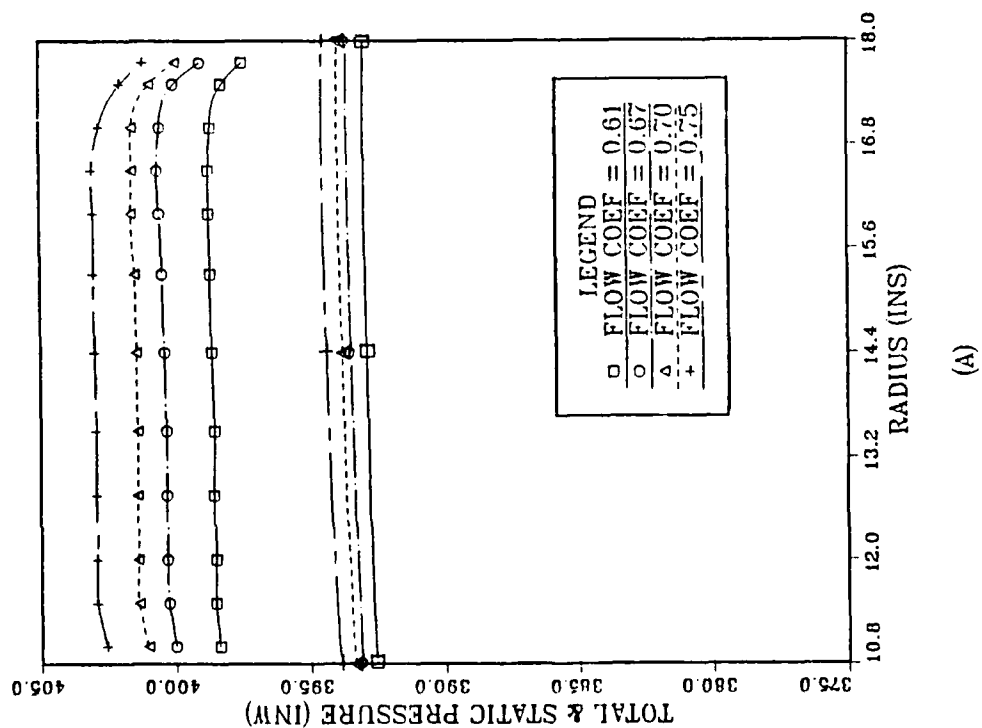
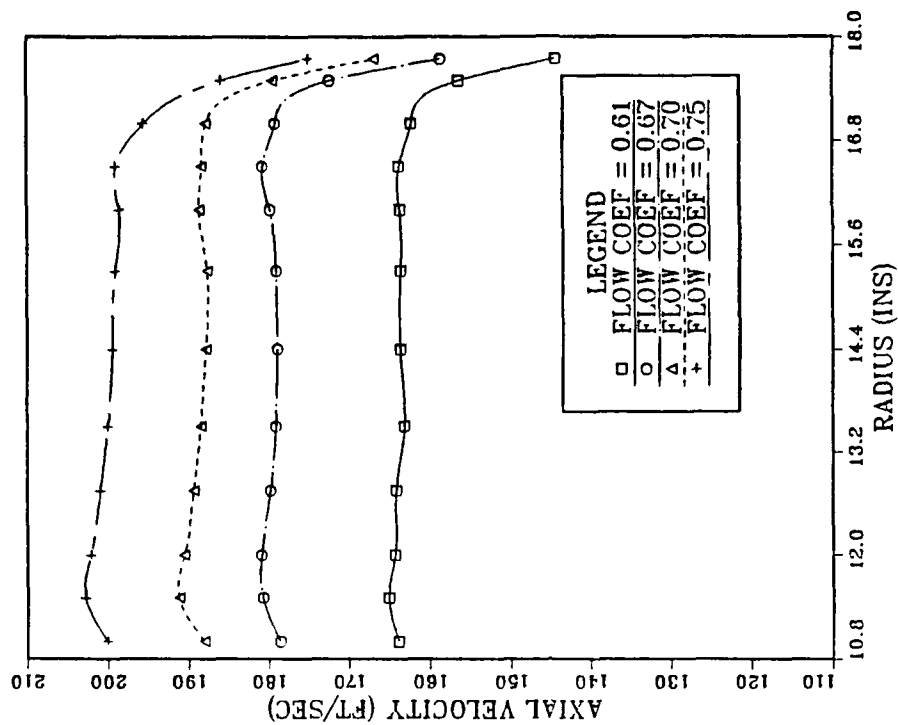


Figure 18. Radial Section of the NPS Compressor



(A)



(B)

Figure 19. Spanwise Distribution of the Flow Properties Measured Ahead of the Inlet Guide Vane

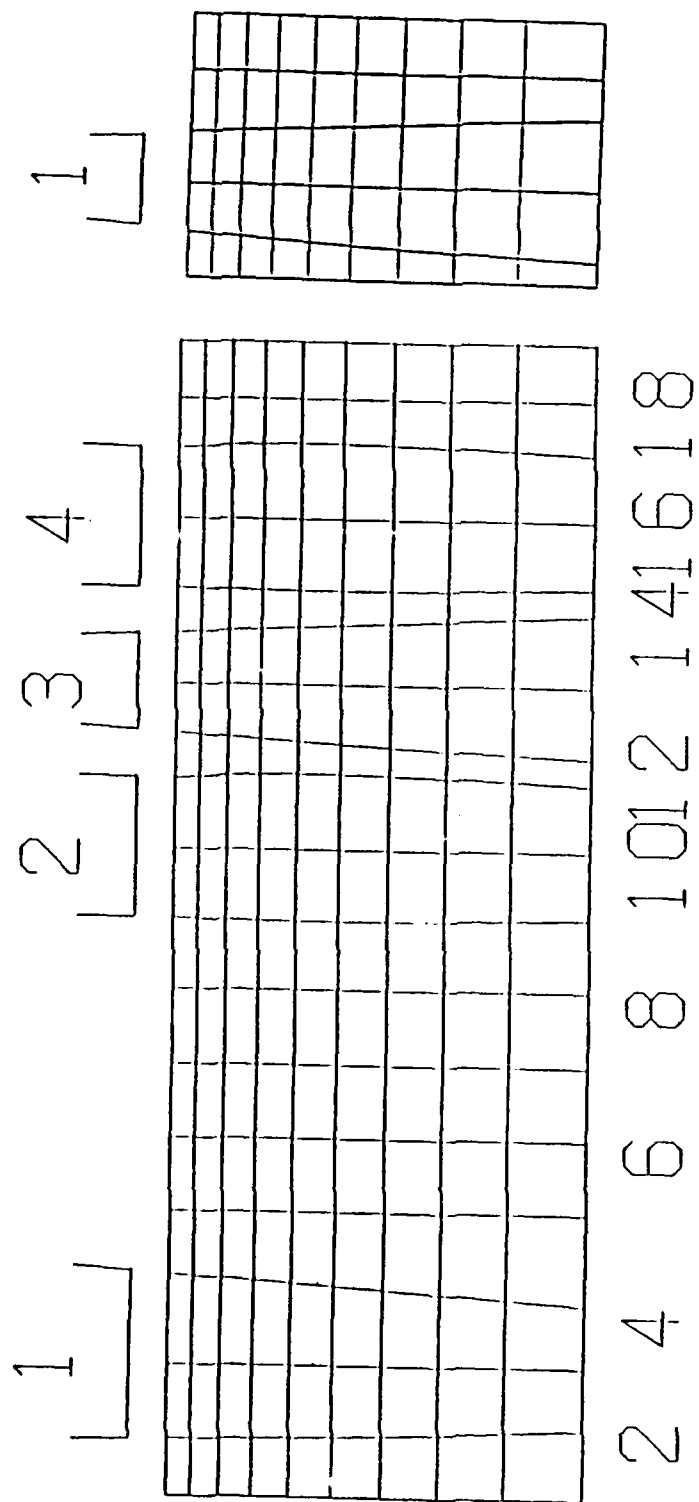


Figure 20. Computational Mesh for the NPS Compressor

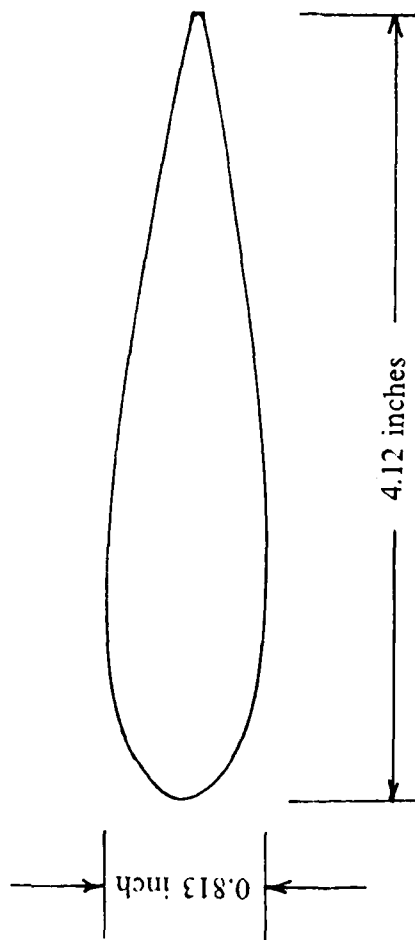
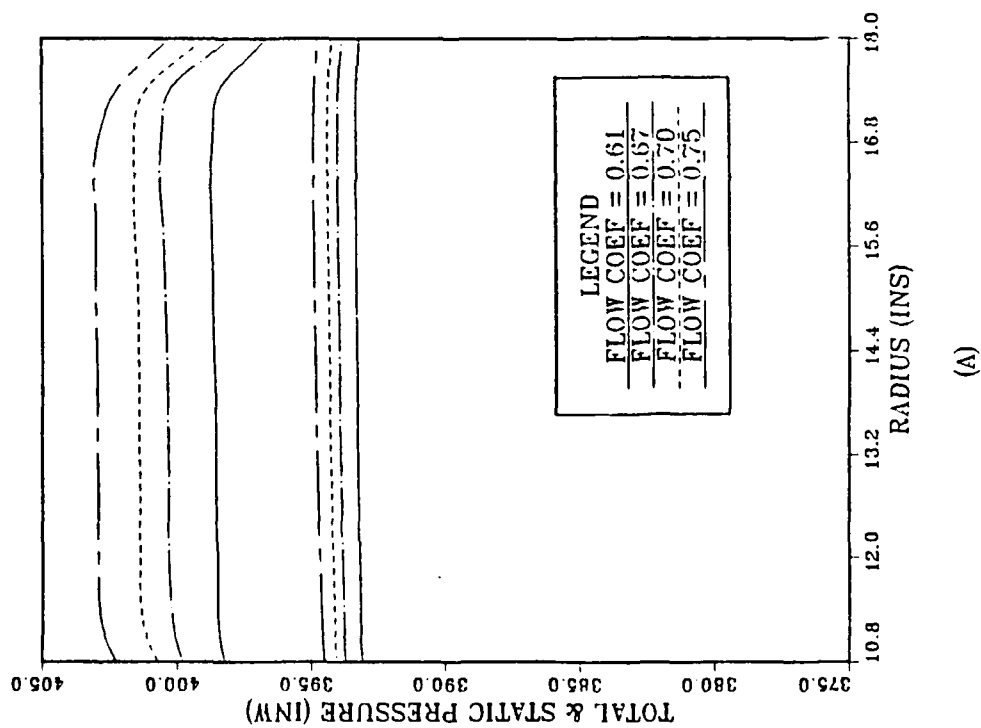
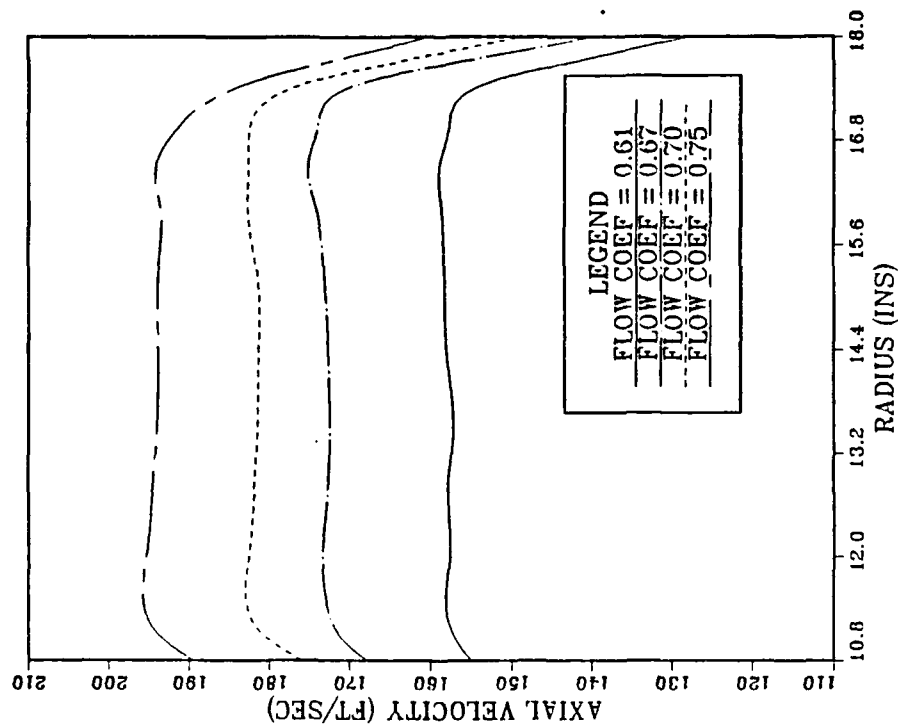


Figure 21. Compressor Strut Section



(A)



(B)

Figure 22. Spanwise Distribution of the Mixed-out Flow Properties Calculated Ahead of the Inlet Guide Vane

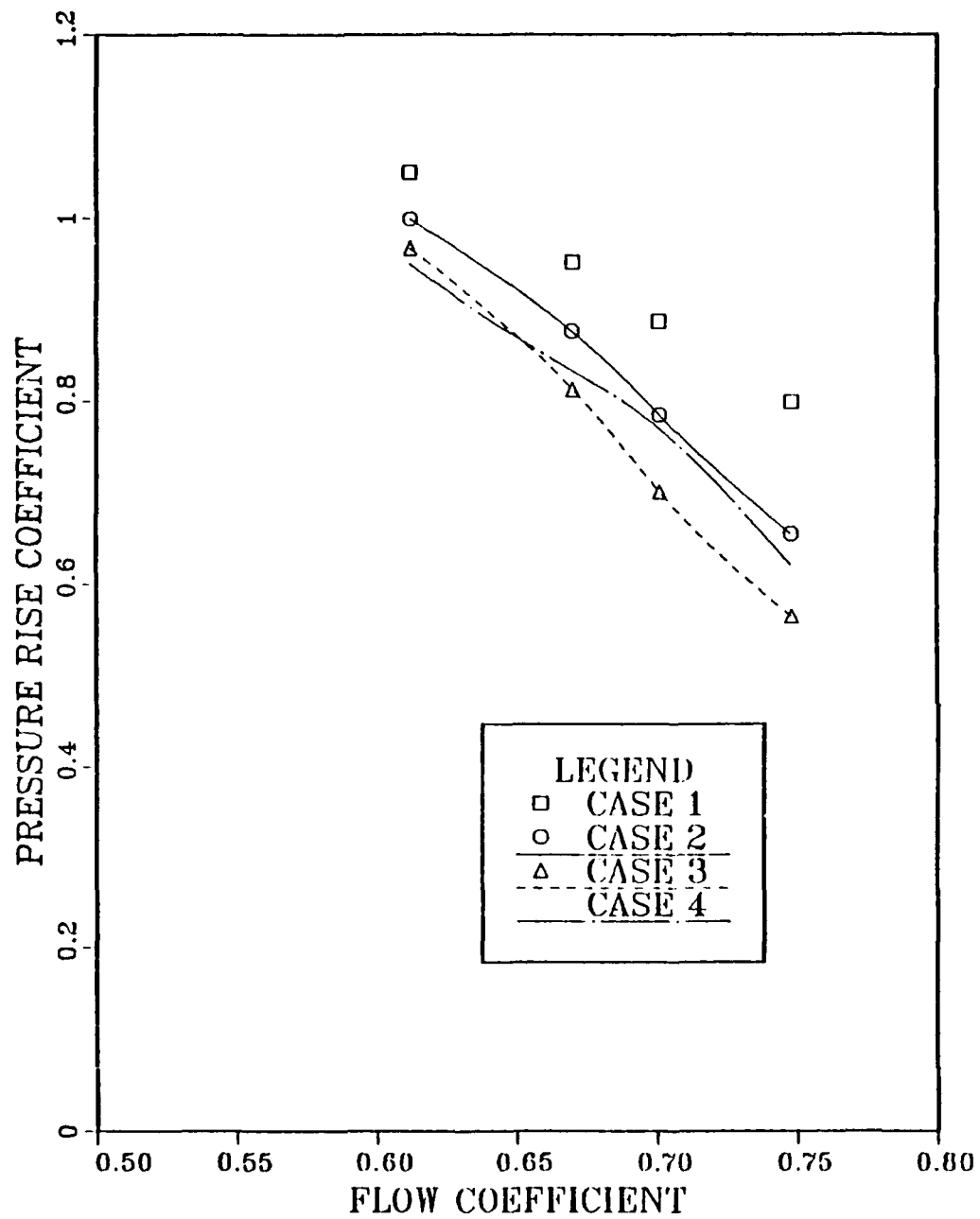


Figure 23. Variation of the Compressor Pressure Rise Coefficient with Flow Coefficient

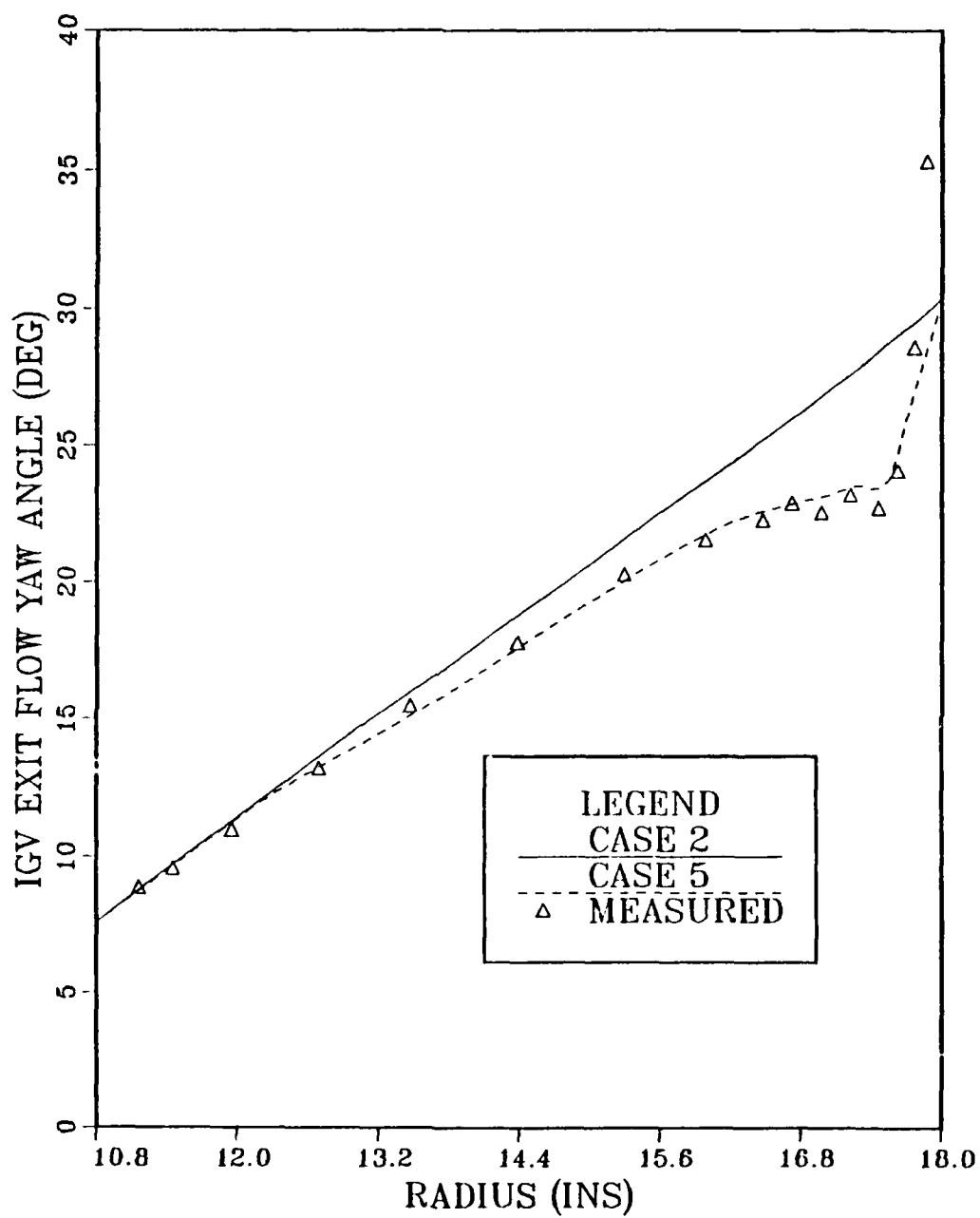


Figure 24. Spanwise Distribution of the Flow Angle from the Inlet Guide Vane

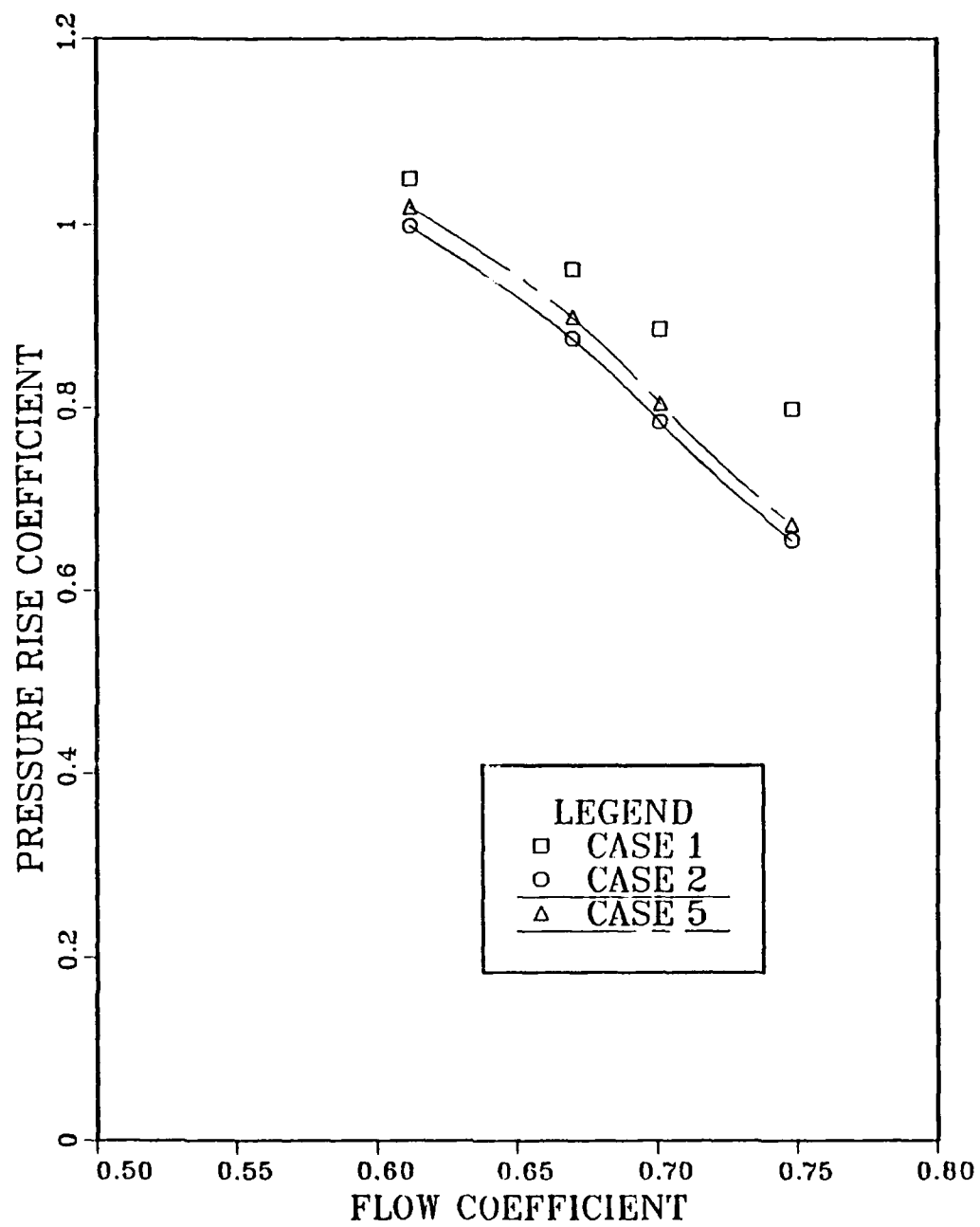


Figure 25. Effect of the Inlet Guide Vane Flow Underturning on the Pressure Rise Coefficient

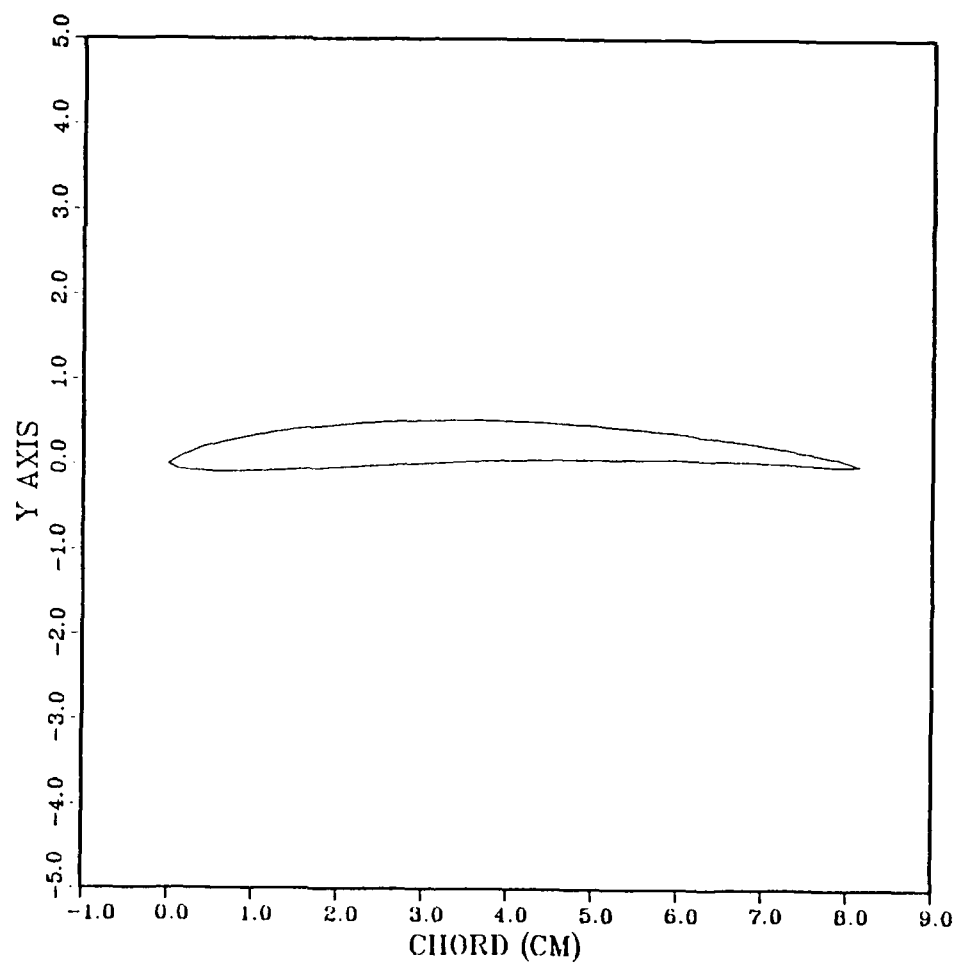


Figure 26. Profile of the Rotor Tip Section

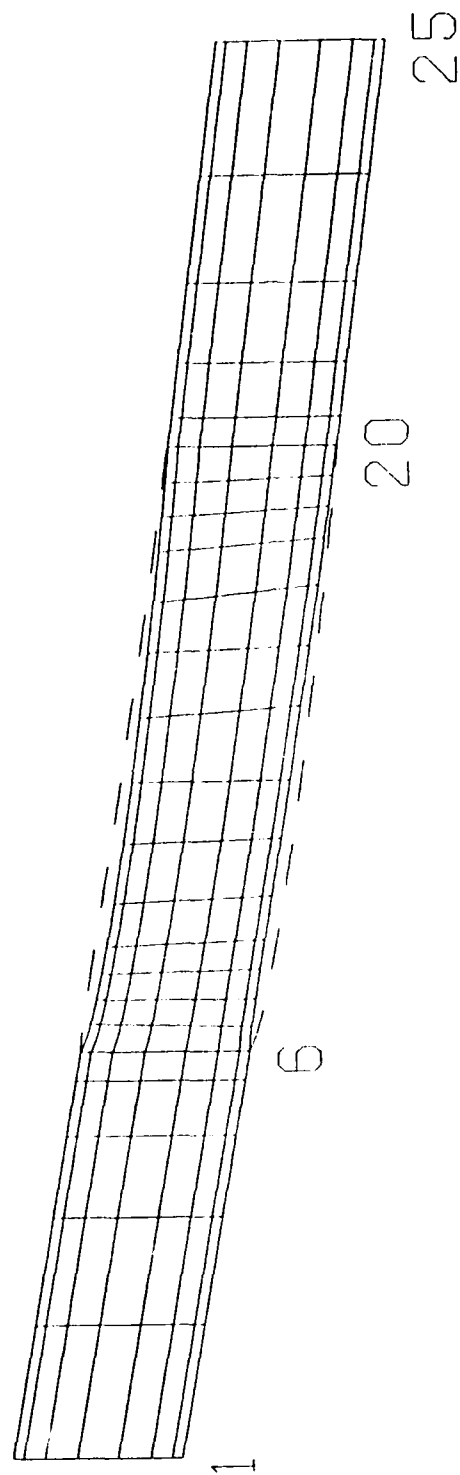


Figure 27. Computational Mesh for the Blade-to-Blade Solution

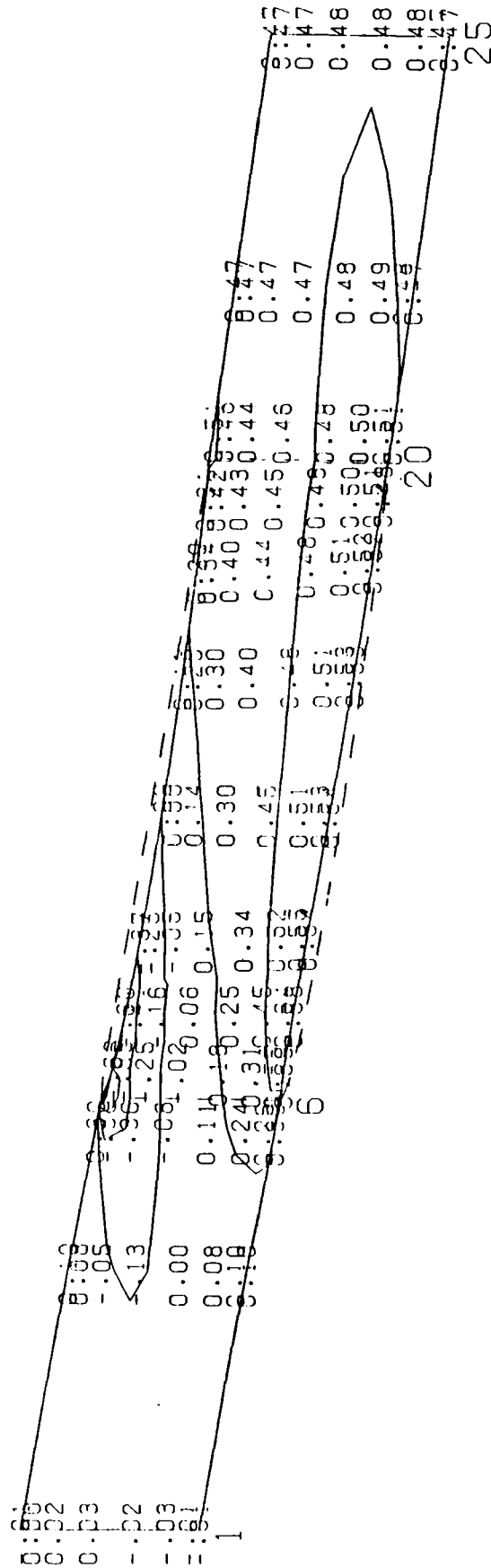


Figure 28. Iso-pressure Lines from the Blade-to-Blade Solution

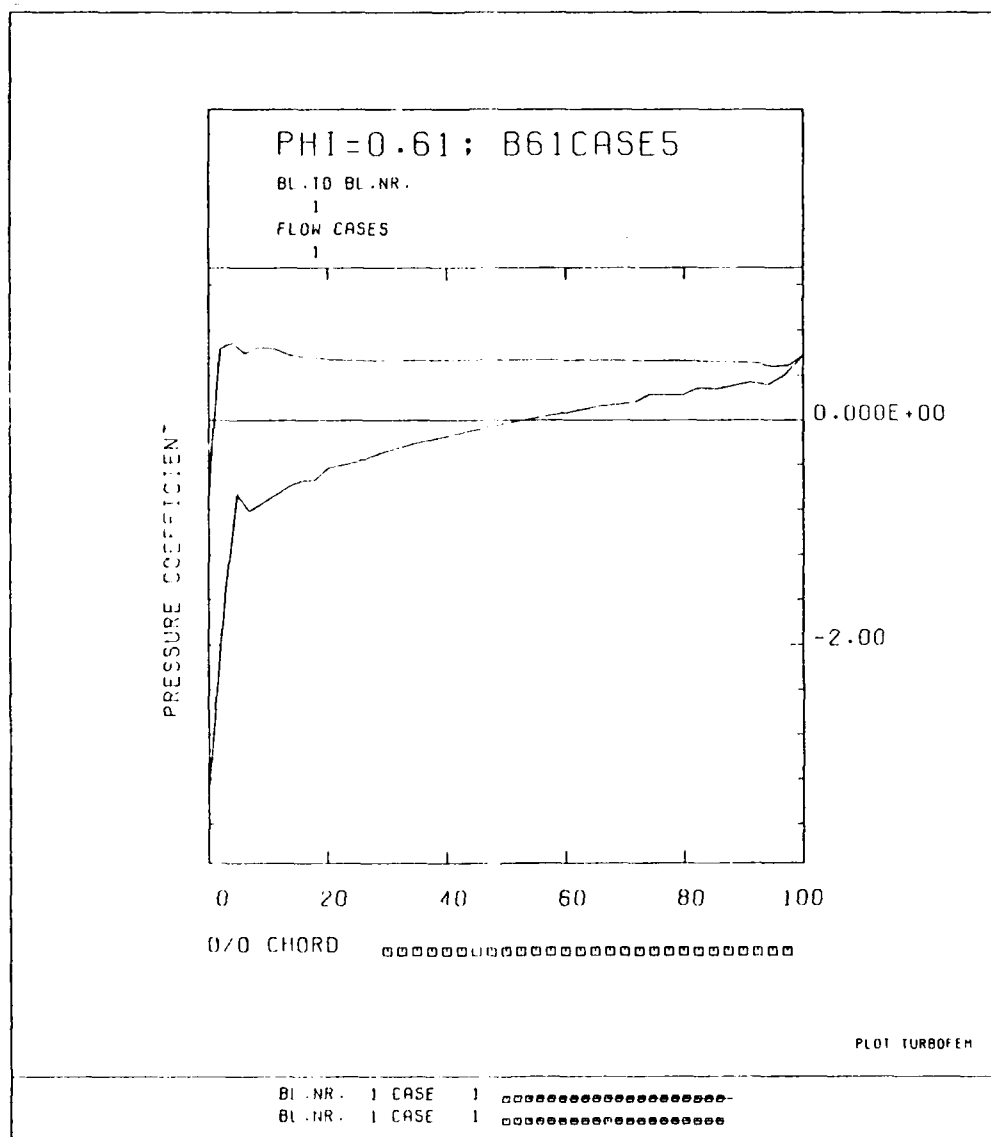


Figure 29. Pressure Coefficients from the Blade-to-Blade Solution

APPENDIX A. DERIVATION OF THE RELATIVE THROUGHFLOW EQUATION FOR Q3DFLO'81

The steady, relative equation of motion (Eq. 18), is

$$\vec{W} \times (\nabla \times \vec{V}) = T\nabla_R S - \nabla_R I + \vec{F}_b + \vec{F}_f \quad \{18\}$$

The two force terms \vec{F}_b and \vec{F}_f are eliminated from Eq. (18) by projecting Eq. (18) in the direction of $\vec{F}_b \times \vec{W}$. Since \vec{F}_f is opposite in direction to \vec{W}

$$(\vec{F}_b \times \vec{W}) \cdot \vec{F}_f = 0 \quad \{20\}$$

and, clearly

$$(\vec{F}_b \times \vec{W}) \cdot \vec{F}_b = 0 \quad \{21\}$$

Hence, the balance of Eq. (18) becomes

$$-(\vec{F}_b \times \vec{W}) \cdot \vec{W} \times (\nabla \times \vec{V}) = (\vec{F}_b \times \vec{W}) \cdot (T\nabla_R S - \nabla_R I) \quad \{22\}$$

Next, Eq. (22) is expressed in cylindrical coordinates. This is done term by term.

Step 1: Expanding $\vec{F}_b \times \vec{W}$ gives

$$\vec{F}_b \times \vec{W} = \vec{i}_r(F_{b\theta}W_z - F_{bz}W_\theta) + \vec{i}_\theta(F_{bz}W_r - F_{br}W_z) + \vec{i}_z(F_{br}W_\theta - F_{b\theta}W_r) \quad \{23\}$$

Step 2: $T\nabla_R S - \nabla_R I$ on the RHS of Eq. (22) becomes

$$T\nabla_R S - \nabla_R I = \vec{i}_r\left(T\frac{\partial S}{\partial r} - \frac{\partial I}{\partial r}\right) + \vec{i}_\theta\frac{1}{r}\left(T\frac{\partial S}{\partial \theta} - \frac{\partial I}{\partial \theta}\right) + \vec{i}_z\left(T\frac{\partial S}{\partial z} - \frac{\partial I}{\partial z}\right) \quad \{24\}$$

Since the model assumes axisymmetric flow by averaging the flow properties across the blade passage

$$\frac{1}{r} \frac{\partial(\dots)}{\partial \theta} = 0 \quad \{25\}$$

and Eq. (24) is reduced to

$$T\nabla_R S - \nabla_R I = \vec{i}_r (T \frac{\partial S}{\partial r} - \frac{\partial I}{\partial r}) + \vec{i}_z (T \frac{\partial S}{\partial z} - \frac{\partial I}{\partial z}) \quad \{26\}$$

Step 3: Using Eq. (23) and Eq. (26), the RHS of Eq. (22) becomes

$$\begin{aligned} (\vec{F}_b \times \vec{W}) \cdot (T\nabla_R S - \nabla_R I) &= (F_{b\theta} W_z - F_{bz} W_\theta) (T \frac{\partial S}{\partial r} - \frac{\partial I}{\partial r}) \\ &+ (F_{br} W_\theta - F_{b\theta} W_r) (T \frac{\partial S}{\partial z} - \frac{\partial I}{\partial z}) \end{aligned} \quad \{27\}$$

Step 4: Since

$$\nabla \times \vec{V} = \vec{i}_r \frac{1}{r} \left(\frac{\partial V_z}{\partial \theta} - \frac{\partial(rV_\theta)}{\partial z} \right) + \vec{i}_\theta \left(\frac{\partial V_r}{\partial z} - \frac{\partial V_z}{\partial r} \right) + \vec{i}_z \frac{1}{r} \left(\frac{\partial(rV_\theta)}{\partial r} - \frac{\partial V_r}{\partial \theta} \right) \quad \{28\}$$

using Eq. (25),

$$\nabla \times \vec{V} = -\vec{i}_r \frac{1}{r} \frac{\partial(rV_\theta)}{\partial z} + \vec{i}_\theta \left(\frac{\partial V_r}{\partial z} - \frac{\partial V_z}{\partial r} \right) + \vec{i}_z \frac{1}{r} \frac{\partial(rV_\theta)}{\partial r} \quad \{29\}$$

therefore

$$\begin{aligned} \vec{W} \times (\nabla \times \vec{V}) &= \vec{i}_r \left(\frac{W_\theta}{r} \frac{\partial(rV_\theta)}{\partial r} - W_z \left(\frac{\partial V_r}{\partial z} - \frac{\partial V_z}{\partial r} \right) \right) \\ &+ \vec{i}_\theta \left(\frac{W_z}{r} \frac{\partial(rV_\theta)}{\partial z} - \frac{W_r}{r} \frac{\partial(rV_\theta)}{\partial r} \right) \\ &+ \vec{i}_z \left(W_r \left(\frac{\partial V_r}{\partial z} - \frac{\partial V_z}{\partial r} \right) - \frac{W_\theta}{r} \frac{\partial(rV_\theta)}{\partial z} \right) \end{aligned} \quad \{30\}$$

Since there is no difference in magnitude and direction between V_z and W_z and V_r and W_r , Eq. (30) can also be expressed as

$$\begin{aligned} \vec{W} \times (\nabla \times \vec{V}) &= \vec{i}_r \left(\frac{W_\theta}{r} \frac{\partial(rV_\theta)}{\partial r} - W_z \left(\frac{\partial W_r}{\partial z} - \frac{\partial W_z}{\partial r} \right) \right) \\ &+ \vec{i}_\theta \left(\frac{W_z}{r} \frac{\partial(rV_\theta)}{\partial z} - \frac{W_r}{r} \frac{\partial(rV_\theta)}{\partial r} \right) \\ &+ \vec{i}_z \left(W_r \left(\frac{\partial W_r}{\partial z} - \frac{\partial W_z}{\partial r} \right) - \frac{W_\theta}{r} \frac{\partial(rV_\theta)}{\partial z} \right) \end{aligned} \quad \{31\}$$

Step 5: Using Eq. (23) and Eq. (31), the LHS of Eq. (22) becomes

$$\begin{aligned}
 (\vec{F}_b \times \vec{W}) \cdot \vec{W} \times (\nabla \times \vec{V}) &= (F_{b\theta} W_z - F_{bz} W_\theta) \left(\frac{W_\theta}{r} \frac{\partial(rV_\theta)}{\partial r} - W_z \left(\frac{\partial W_r}{\partial z} - \frac{\partial W_z}{\partial r} \right) \right) \\
 &+ (F_{bz} W_r - F_{br} W_z) \left(\frac{W_z}{r} \frac{\partial(rV_\theta)}{\partial z} - \frac{W_r}{r} \frac{\partial(rV_\theta)}{\partial r} \right) \\
 &+ (F_{br} W_\theta - F_{b\theta} W_r) \left(W_r \left(\frac{\partial W_r}{\partial z} - \frac{\partial W_z}{\partial r} \right) - \frac{W_\theta}{r} \frac{\partial(rV_\theta)}{\partial z} \right)
 \end{aligned} \quad \{32\}$$

Re-arranging,

$$\begin{aligned}
 (\vec{F}_b \times \vec{W}) \cdot \vec{W} \times (\nabla \times \vec{V}) &= \left(\frac{\partial W_z}{\partial r} - \frac{\partial W_r}{\partial z} \right) (F_{b\theta} W_z^2 - F_{bz} W_\theta W_z + F_{b\theta} W_r^2 - F_{br} W_\theta W_r) \\
 &+ \frac{1}{r} \frac{\partial(rV_\theta)}{\partial r} (F_{b\theta} W_z W_\theta - F_{bz} W_\theta^2 - F_{bz} W_r^2 + F_{br} W_z W_r) \\
 &- \frac{1}{r} \frac{\partial(rV_\theta)}{\partial z} (F_{br} W_z^2 - F_{bz} W_r W_z + F_{br} W_\theta^2 - F_{b\theta} W_r W_\theta) \\
 &= \left(\frac{\partial W_z}{\partial r} - \frac{\partial W_r}{\partial z} \right) (F_{b\theta} (W_z^2 + W_r^2) - W_\theta (F_{bz} W_z + F_{br} W_r)) \\
 &+ \frac{1}{r} \frac{\partial(rV_\theta)}{\partial r} (W_z (F_{b\theta} W_\theta + F_{br} W_r) - F_{bz} (W_\theta^2 + W_r^2)) \\
 &+ \frac{1}{r} \frac{\partial(rV_\theta)}{\partial z} (F_{br} (W_z^2 + W_\theta^2) - W_r (F_{bz} W_z + F_{b\theta} W_\theta))
 \end{aligned} \quad \{33\}$$

Substituting $W^2 = W_r^2 + W_\theta^2 + W_z^2$ into Eq. (33) yields

$$\begin{aligned}
 (\vec{F}_b \times \vec{W}) \cdot \vec{W} \times (\nabla \times \vec{V}) &= \left(\frac{\partial W_z}{\partial r} - \frac{\partial W_r}{\partial z} \right) (F_{b\theta} W^2 - W_\theta (F_{bz} W_z + F_{br} W_r)) \\
 &+ \frac{1}{r} \frac{\partial(rV_\theta)}{\partial r} (W_z (F_{b\theta} W_\theta + F_{br} W_r) - F_{bz} W^2) \\
 &+ \frac{1}{r} \frac{\partial(rV_\theta)}{\partial z} (F_{br} W^2 - W_r (F_{bz} W_z + F_{b\theta} W_\theta)) \\
 &= \left(\frac{\partial W_z}{\partial r} - \frac{\partial W_r}{\partial z} \right) (F_{b\theta} W^2 - W_\theta (\vec{F}_b \cdot \vec{W})) \\
 &+ \frac{1}{r} \frac{\partial(rV_\theta)}{\partial r} (W_z (\vec{F}_b \cdot \vec{W}) - F_{bz} W^2) \\
 &+ \frac{1}{r} \frac{\partial(rV_\theta)}{\partial z} (F_{br} W^2 - W_r (\vec{F}_b \cdot \vec{W}))
 \end{aligned} \quad \{34\}$$

Since $\vec{F}_b \cdot \vec{W} = 0$ in Eq. (34), the LHS of Eq. (22) becomes

$$\begin{aligned} & (\vec{F}_b \times \vec{W}) \cdot \vec{W} \times (\nabla \times \vec{V}) = \\ & F_{b\theta} W^2 \left(\left(\frac{\partial W_z}{\partial r} - \frac{\partial W_r}{\partial z} \right) - \frac{1}{r} \frac{F_{bz}}{F_{b\theta}} \frac{\partial(rV_\theta)}{\partial r} + \frac{1}{r} \frac{F_{br}}{F_{b\theta}} \frac{\partial(rV_\theta)}{\partial z} \right) \end{aligned} \quad \{35\}$$

Step 6: From Eq. (27) and Eq. (35), Eq. (22) becomes

$$\begin{aligned} & - \left(\left(\frac{\partial W_z}{\partial r} - \frac{\partial W_r}{\partial z} \right) - \frac{F_{bz}}{F_{b\theta}} \frac{1}{r} \frac{\partial(rV_\theta)}{\partial r} + \frac{F_{br}}{F_{b\theta}} \frac{1}{r} \frac{\partial(rV_\theta)}{\partial z} \right) \\ & = \frac{1}{W^2} \left((W_z - \frac{F_{bz}}{F_{b\theta}} W_\theta) \left(T \frac{\partial S}{\partial r} - \frac{\partial I}{\partial r} \right) + \left(\frac{F_{br}}{F_{b\theta}} W_\theta - W_r \right) \left(T \frac{\partial S}{\partial z} - \frac{\partial I}{\partial z} \right) \right) \end{aligned} \quad \{36\}$$

Step 7: The body force components from Eq. (36) can be eliminated by expressing them in terms of the blade surface angles. Figure 30 shows that,

$$\frac{F_{bz}}{F_{b\theta}} = -\tan \beta \quad \{37\}$$

and

$$\frac{F_{br}}{F_{b\theta}} = \tan \eta \quad \{38\}$$

Substituting Eq. (37) and Eq. (38) into Eq. (36) and re-arranging,

$$\begin{aligned} & \frac{\partial W_z}{\partial r} - \frac{\partial W_r}{\partial z} = \\ & \frac{(W_z + W_\theta \tan \beta) \left(\frac{\partial I}{\partial r} - T \frac{\partial S}{\partial r} \right) + (W_\theta \tan \eta - W_r) \left(\frac{\partial I}{\partial z} - T \frac{\partial S}{\partial z} \right)}{W^2} \\ & - \frac{1}{r} \left(\tan \beta \frac{\partial(rV_\theta)}{\partial r} + \tan \eta \frac{\partial(rV_\theta)}{\partial z} \right) \end{aligned} \quad \{39\}$$

Step 8: Lastly, the streamfunction (ψ) defined through the equations

$$2\pi \frac{\partial \psi}{\partial r} = \rho 2\pi r b W_z \quad \{40\}$$

and

$$2\pi \frac{\partial \psi}{\partial z} = -\rho 2\pi r b W_r \quad \{41\}$$

where b is the tangential blockage ratio, is introduced. The LHS of Eq. (39) can be expressed in terms of ψ by differentiating Eq. (40) and Eq. (41), which yields

$$\frac{\partial W_z}{\partial r} = \frac{\partial}{\partial r} \left(\frac{1}{\rho r b} \frac{\partial \psi}{\partial r} \right) \quad \{42\}$$

and

$$\frac{\partial W_r}{\partial z} = -\frac{\partial}{\partial z} \left(\frac{1}{\rho r b} \frac{\partial \psi}{\partial z} \right) \quad \{43\}$$

Finally, Eq. (19), which is the radial equilibrium equation for the rotor flow, is obtained by substituting Eq. (42) and Eq. (43) into Eq. (39), yielding

$$\begin{aligned} & \frac{\partial}{\partial r} \left(\frac{1}{\rho r b} \frac{\partial \psi}{\partial r} \right) + \frac{\partial}{\partial z} \left(\frac{1}{\rho r b} \frac{\partial \psi}{\partial z} \right) = \\ & \frac{(W_z + W_\theta \tan \beta) \left(\frac{\partial I}{\partial r} - T \frac{\partial S}{\partial r} \right) + (W_\theta \tan \eta - W_r) \left(\frac{\partial I}{\partial z} - T \frac{\partial S}{\partial z} \right)}{W^2} \\ & - \frac{1}{r} \left(\tan \beta \frac{\partial(rV_\theta)}{\partial r} + \tan \eta \frac{\partial(rV_\theta)}{\partial z} \right) \end{aligned} \quad \{44\}$$

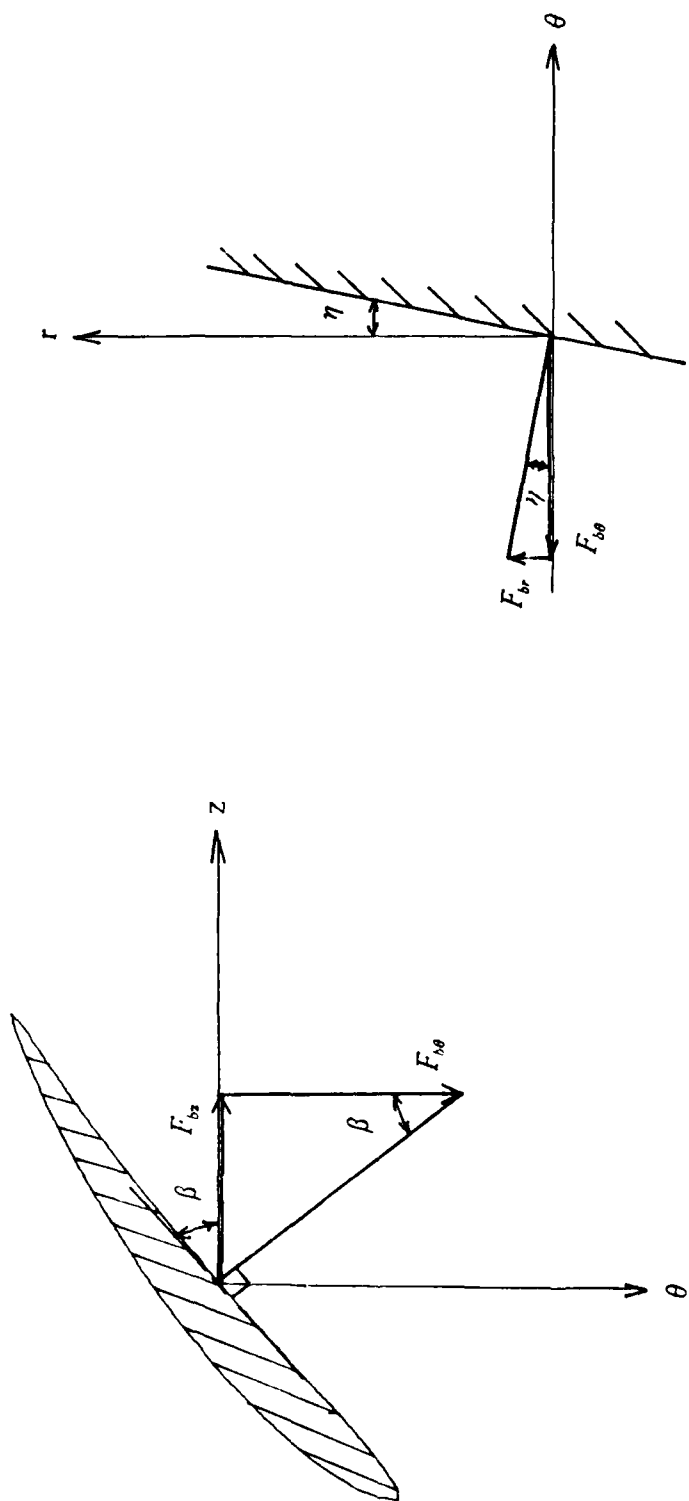


Figure 30. Relationship between Blade Surface Angles and Body Forces

APPENDIX B. CALCULATION OF THE MIXED-OUT CONDITION FOR THE STRUT WAKES

The process of the diffusion and mixing of the strut wake on an axisymmetric stream surface at a constant radial position can be modelled as constant area two-dimensional mixing of two streams initially separated by the wake thickness (δ^*) as shown in Figure 31. Since the flow Mach number is less than 0.2, the velocity and total pressure after mixing can be determined by assuming the flow to be incompressible. By conservation of mass,

$$\rho(s - \delta^*)V_1 = \rho s V_2 \quad \{45\}$$

so that

$$V_2 = (1 - \frac{\delta^*}{s}) V_1 \quad \{46\}$$

Using the definition of blockage factor (k)

$$k = (1 - \frac{\delta^*}{s}) \quad \{47\}$$

Eq. (46) becomes

$$V_2 = k V_1 \quad \{48\}$$

By conservation of momentum,

$$(P_1 - P_2)s + \rho(s - \delta^*)V_1^2 - \rho s V_2^2 = 0 \quad \{49\}$$

Using Eq. (46), Eq. (49) becomes

$$(P_1 - P_2)s + \rho(s - \delta^*)V_1^2 - \rho s (1 - \frac{\delta^*}{s})^2 V_1^2 = 0 \quad \{50\}$$

Re-arranging,

$$(P_2 - P_1) = \rho(1 - \frac{\delta^*}{s})V_1^2(1 - (1 - \frac{\delta^*}{s})) \quad \{51\}$$

Using Eq. (47), Eq. (51) becomes

$$(P_2 - P_1) = \rho V_1^2 (k - (1 - k)) \quad \{52\}$$

From the definition of total pressure

$$P_{t1} = P_1 + \frac{1}{2} \rho V_1^2 \quad \{53\}$$

and

$$P_{t2} = P_2 + \frac{1}{2} \rho V_2^2 \quad \{54\}$$

Using Eq. (48), Eq. (54) becomes

$$P_{t2} = P_2 + \frac{1}{2} \rho V_1^2 k^2 \quad \{55\}$$

Subtracting Eq. (53) from Eq. (55)

$$(P_{t2} - P_{t1}) = (P_2 - P_1) + \frac{1}{2} \rho V_1^2 (k^2 - 1) \quad \{56\}$$

Using Eq. (52), Eq. (56) becomes

$$(P_{t2} - P_{t1}) = \rho V_1^2 (k - (1 - k)) + \frac{1}{2} \rho V_1^2 (k^2 - 1) \quad \{57\}$$

Re-arranging,

$$P_{t2} = P_{t1} - \frac{1}{2} \rho V_1^2 (1 - 2k + k^2) \quad \{58\}$$

or

$$P_{t2} = P_{t1} - \frac{1}{2} \rho V_1^2 (1 - k)^2 \quad \{59\}$$

Hence, the velocity and total pressure after diffusion and mixing of the strut wakes can be calculated by using Eq. (46) and Eq. (59) respectively.

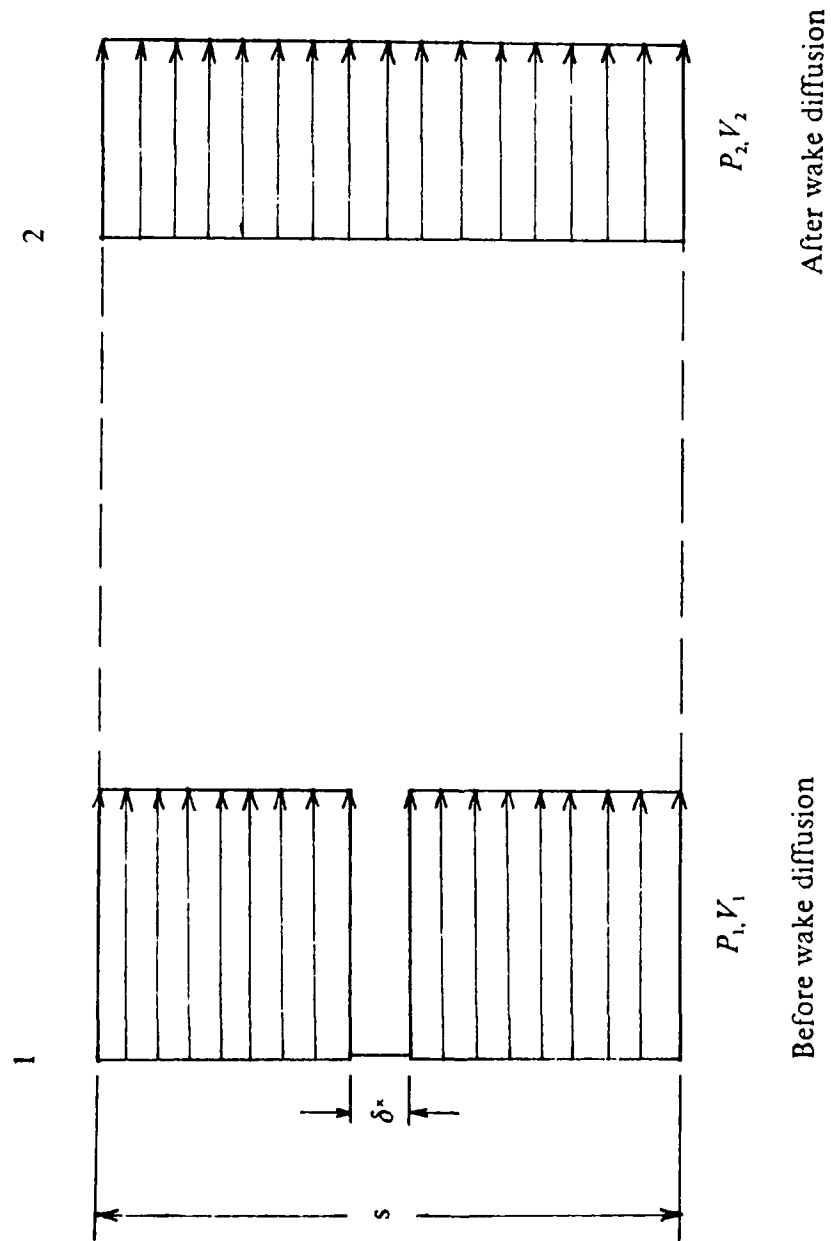


Figure 31. Schematic for Constant Area Mixing Calculation for the Strut Wakes

LIST OF REFERENCES

1. Naval Postgraduate School Report NPS67-84-022, *Computational Models for Turbomachinery Flows*, by Hirsch, C., Dec 1984.
2. *Computer Program for Turbomachinery Flows - Finite Element Method, General Principles*, Numeca, Brussels, 1981.
3. Vavra, M. H., *Aerothermodynamics and Flow in Turbomachines*, Wiley, New York, May 1974.
4. Naval Postgraduate School Report NPS67-84-005, *Application of Finite Element Code Q3DFLO'81 to Turbomachinery flow Fields*, by Schulz, H. D., and others, Sep 1984.
5. United Technologies Research Center Report N00014-84-C-0354 , *An Assessment of Single- and Multi- Stage Compressor Flow Modeling- Part 1 Design Conditions*, by Dring, R. P. and Joslyn, M. D., Jul 1985.
6. Dring, R. P., *Technical Briefs - Blockage in Axial Compressors*, Journal of Engineering for Gas Turbines and Power, Vol. 106, Jul 1984.
7. Naval Postgraduate School Report NPS-57VA70091A, *Aerodynamic Design of Symmetrical Blading for Three-Stage Axial Flow Compressor Test Rig*, by Vavra, M.H., Sep 1970.
8. Naval Postgraduate School Report NPS-57VA73121A, *Redesign of the Low Speed Three Stage Axial Flow Compressor Test Facility*, by Vavra, M.H., Pucci, P.F., Schlachter W., Dec 1973.
9. Naval Postgraduate School Report NPS-67-86-003CR, *Single Stage Compressor Test Baseline for a Symmetric Blading*, by Moyle, I.N., Dec 1986.

10. Tarigan, M., *Development of a Boundary Layer Control Device for Tip Clearance Experiments in an Axial Compressor*, Master's Thesis, Naval Postgraduate School, Monterey, California, Mar 1988.
11. Waddell, L. W., *Evaluation of the Performance and Flow in an Axial Compressor*, Master's Thesis, Naval Postgraduate School, Monterey, California, Mar 1982.

INITIAL DISTRIBUTION LIST

		No. Copies
1.	Defense Technical Information Center Cameron Station Alexandria, VA 22304-6145	2
2.	Library, Code 0142 Naval Postgraduate School Monterey, CA 93943-5002	2
3.	Commander Naval Air Systems Command Washington, D. C. 20361 Attn: Code AIR 931	1
4.	Commander Naval Air Systems Command Washington, D. C. 20361 Attn: Code AIR 931E	1
5.	Commander Naval Air Systems Command Washington, D. C. 20361 Attn: Code AIR 530	1
6.	Commander Naval Air Systems Command Washington, D. C. 20361 Attn: Code AIR 536	1
7.	Commander Naval Air Systems Command Washington, D. C. 20361 Attn: Code AIR 00D	1
8.	Office of Naval Research 800 N. Quincy Street Arlington, VA 22217 Attn: Code 113	1
9.	Commanding Officer Naval Air Propulsion Center Trenton, N. J. 08628 Attn: G. Mangano, PE-31	1

- | | | |
|-----|---|----|
| 10. | National Aeronautics and Space Administration
Lewis Research Center
21000 Brookpark Road
Cleveland, OH 44135
Attn: N. Sanger, MS 5-11 | 1 |
| 11 | Prof. Dr. Ir. Charles Hirsch
Faculteit Toegepaste Wetenschappen
Dienst Stromingsmechanica
Vrije Universiteit Brussel
Pleinlaan 2
1050 Brussel, Belgium | 1 |
| 12 | Dr. Robert R. Dring
United Technologies Research Center
East Hartford, CT. 06108 | 1 |
| 13. | Naval Postgraduate School
Monterey, California 93943-5000
Attn: Chairman, Department of Aeronautics and Astronautics (67) | 1 |
| 14. | Naval Postgraduate School
Monterey, California 93943-5000
Attn: Professor Max. F. Platzer (67PL) | 1 |
| 15. | Naval Postgraduate School
Monterey, California 93943-5000
Attn: Professor Raymond P. Shreeve (67SI) | 10 |
| 16 | Yeo, Peng Hian
Block 14, Tiong Bahru Road
#02-128, Postal District 0316
Republic of Singapore | 3 |